



Theory of mechanochemical patterning and optimal migration in cell monolayers

Daniel Boocock^{1,5}, Naoya Hino^{2,5}, Natalia Ruzickova¹, Tsuyoshi Hirashima^{3,4}✉ and Edouard Hannezo¹✉

Collective cell migration offers a rich field of study for non-equilibrium physics and cellular biology, revealing phenomena such as glassy dynamics, pattern formation and active turbulence. However, how mechanical and chemical signalling are integrated at the cellular level to give rise to such collective behaviours remains unclear. We address this by focusing on the highly conserved phenomenon of spatiotemporal waves of density and extracellular signal-regulated kinase (ERK) activation, which appear both *in vitro* and *in vivo* during collective cell migration and wound healing. First, we propose a biophysical theory, backed by mechanical and optogenetic perturbation experiments, showing that patterns can be quantitatively explained by a mechanochemical coupling between active cellular tensions and the mechanosensitive ERK pathway. Next, we demonstrate how this biophysical mechanism can robustly induce long-ranged order and migration in a desired orientation, and we determine the theoretically optimal wavelength and period for inducing maximal migration towards free edges, which fits well with experimentally observed dynamics. We thereby provide a bridge between the biophysical origin of spatiotemporal instabilities and the design principles of robust and efficient long-ranged migration.

The collective dynamics of cell migration has been a topic of intense interest for biologists and physicists alike, due, on the one hand, to its crucial role in embryonic development, wound healing, homeostasis and cancer invasion^{1–4} and, on the other hand, to it being a prime experimental example of complex dynamics in out-of-equilibrium physics^{5,6}. Epithelial cells consume energy to drive their collective migration, exerting forces on substrates that are also transmitted to neighbouring cells via adhesive complexes. Elegant *in vitro* experiments have revealed a wealth of intricate collective dynamics resulting from these ingredients, ranging from long-ranged directed migration and fingering instabilities towards free edges^{7,8} to glassy dynamics⁹, active turbulence¹⁰ and spatiotemporal density waves^{11–17}. Thus, epithelial monolayers are an ideal model system for active matter, and a number of theoretical studies have aimed to model these complex dynamics, in particular by concentrating on the mechanical and hydrodynamical properties of epithelial monolayers^{11,14–22}. However, a unified picture of the mechanical and biochemical couplings occurring through cell–cell and cell–substrate interactions is still lacking⁶.

In particular, whether and how the internal state, that is, biochemical signalling, of individual cells influences the resulting dynamics remains less explored, both theoretically and experimentally. This is in part due to the practical challenges involved in assessing live protein activity with high temporal resolution, although recently the development of Förster resonance energy transfer (FRET) biosensors^{23,24} has begun to alleviate some of these difficulties. Imaging monolayer movements together with ERK/MAP kinase activity (MAP, mitogen-activated protein) has for instance revealed that the aforementioned spatiotemporal waves in cell density are accompanied by corresponding waves of chemical activity (with ERK activity locally anti-correlated to cell density)²⁵. Strikingly, such ERK waves were also observed *in vivo* during wound healing in mouse skin²⁶.

Given that the ERK pathway is a central signalling platform, able to integrate and modulate mechanical forces^{25,27–30}, these observations raise the intriguing possibility that mutual mechanochemical feedback loops could generically control this behaviour^{14,31,32}. Thus, we aim to uncover (1) how these coupled waves arise from a theoretical standpoint, (2) the biological mechanisms through which mechanical and ERK waves are linked, and (3) whether they have any functional role in collective migration and wound healing. Indeed, long-range ordering of migration forces is a striking feature of epithelial tissues⁸, and while this has been proposed to arise via flocking-like mechanisms³³, coordination through mechanochemical waves would be an elegant alternative mechanism²⁷.

Here, we propose a biophysical model of collective motion in epithelial tissues, coupling the mechanics of monolayers to the mechanosensitive dynamics of ERK activity, both from first principles and experimental observations²⁷. We uncover a mechanochemical instability that produces complex spatiotemporal patterns of cell density, cell velocity and ERK activity at a finite temporal period and length scale. We test the model and fit all of its parameters through analysis of independent optogenetic and mechanical stretching experiments of Madin–Darby canine kidney (MDCK) monolayers²⁷, to provide parameter-free quantitative predictions of multiple features observed in experiments including the period and wavelength of instability. Next, by coupling this instability to cell polarization, we identify a theoretical optimum wavelength and period for inducing maximal polarity (that is, polar traction forces) in the direction of free edges. Strikingly, this optimal pattern is close to those observed both *in vitro* in MDCK layers^{25,27} and *in vivo* in mouse skin wound healing²⁶. Finally, we challenge the model through genetic and pharmacological perturbation experiments and discuss possible implications of this theory in other biological settings.

¹Institute of Science and Technology Austria, Klosterneuburg, Austria. ²Laboratory of Bioimaging and Cell Signaling, Graduate School of Biostudies, Kyoto University, Kyoto, Japan. ³Department of Pathology and Biology of Diseases, Graduate School of Medicine, Kyoto University, Kyoto, Japan. ⁴Japan Science and Technology Agency, PRESTO, Kyoto, Japan. ⁵These authors contributed equally: Daniel Boocock, Naoya Hino. ✉e-mail: hirashima.tsuyoshi.2m@kyoto-u.ac.jp; edouard.hannezo@ist.ac.at

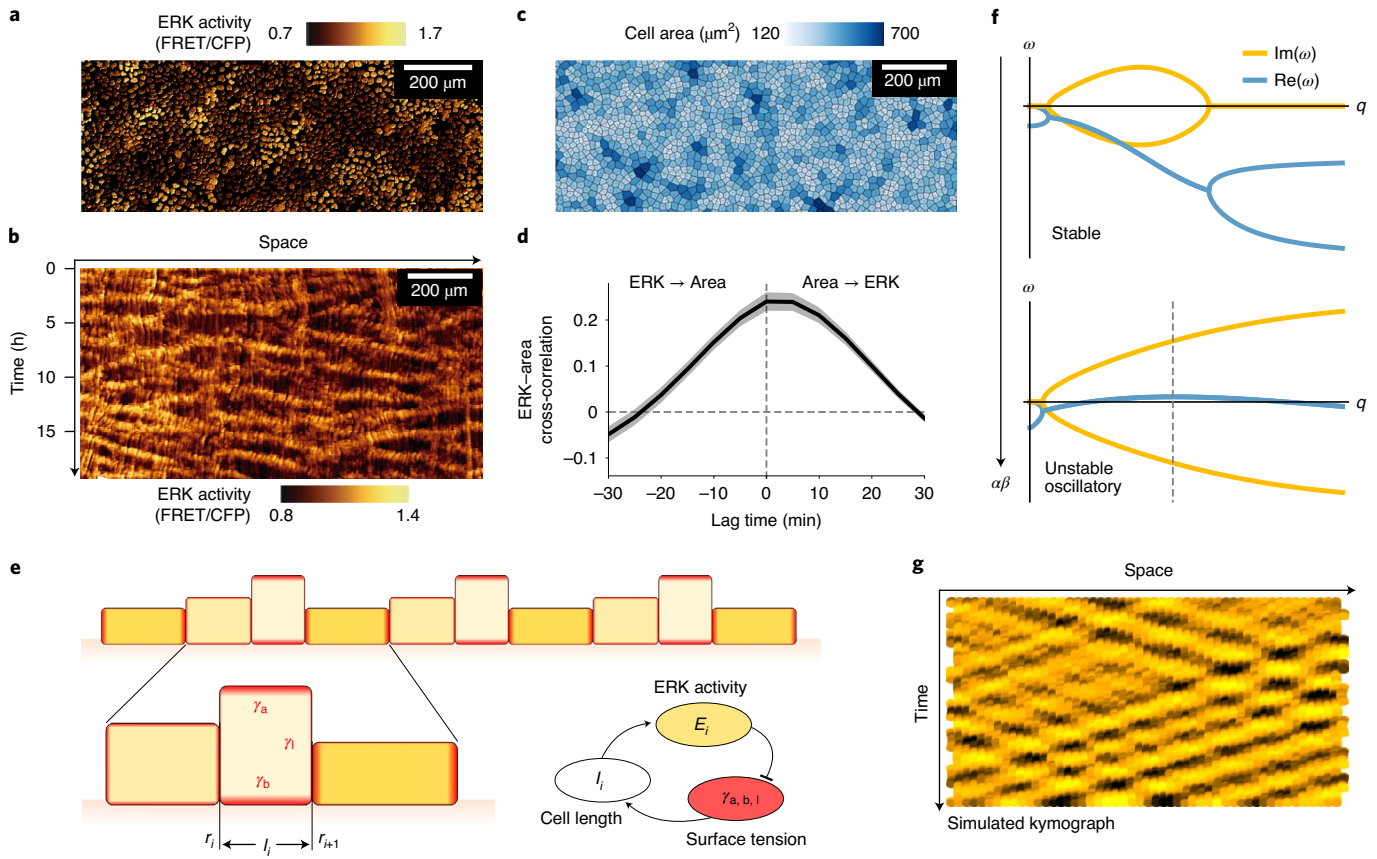


Fig. 1 | Observation and theory of spatiotemporal patterns in confluent cell monolayers. **a–c**, Confluent MDCK monolayers display isotropic patterns of ERK activity (**a** and **b**, kymograph) and density (**c**, colour code indicates cell area from Voronoi tessellation) in contrast to directional waves reported in migrating monolayers. See also Supplementary Video 1. **d**, Cross-correlation function of cell area and ERK activity (defined in the Methods) indicates a positive correlation between the two²⁵, with ERK trailing area by around 3–5 min (ref. ²⁷) (average of $N = 3$ experiments, shaded areas indicate standard deviation). **e**, Schematic of our mechanochemical model. ERK activation (yellow) causes actomyosin remodelling (red), differentially affecting apical–basal and lateral tensions $\gamma_{a,b}$. The dependence of ERK activation on cell length l completes a mechanochemical feedback loop between ERK activation, cortical tensions and cell aspect ratio. **f**, Linear stability of this model (equation (4)) reveals a finite wavelength oscillation ($\text{Re}(\omega) > 0$, dashed line) above a certain strength $\alpha\beta_{\text{crit}}$ of mechanochemical coupling. **g**, This instability is confirmed in numerical simulations of the model (kymograph).

Results

Firstly, in agreement with previous studies of expanding MDCK monolayers^{25,27,34}, we confirmed that directional waves of cellular density and ERK activity propagate away from leading edges towards the centre of colonies (Extended Data Fig. 1a,b). Moreover, we performed the same experiments at full two-dimensional (2D) confluence (Fig. 1a–d and Supplementary Video 1) and found similar patterns of ERK and cell density (with ERK positively correlated with, and slightly lagging behind, 2D cell area), although in this case they displayed random orientation of propagation. This suggests that monolayer expansion (mediated by leading edges) is not required for wave formation, motivating us to first study theoretically how isotropic waves of ERK and density arise in the confluent setting.

For this, we first wrote down a minimal model of epithelial monolayer mechanics that we highlight here (see Supplementary Section I for details). The 3D shape of MDCK cells, like in other epithelial tissues, is proposed to arise from a balance of forces between the active stresses generated by actomyosin cortices at the apical, lateral and basal surfaces^{35–37} (resp. denoted as γ_a , γ_l and γ_b). For a single cell on a flat surface, equilibrium of these forces requires that the in-plane length of a cell l is equal to a ratio of active tensions, such that $l \propto (\frac{\gamma_l}{\gamma_a + \gamma_b})^{1/3}$. However, for confluent, heterogeneous

epithelial tissues, cell–cell junctions impose mechanical couplings between cells³⁸, so that the mechanical state of each cell influences the shape, density and velocity of its neighbours³⁹. To describe this we consider, in a simple 1D setting, a linear chain of coupled cells with vertex positions \mathbf{r}_i and surface tensions γ_i (Fig. 1e). If a given cell contracts, it imposes a stress on its neighbours, which is resisted by cellular tensions, as well as by frictional forces with the substrate $\mathbf{f}_i = -\zeta \mathbf{v}_i$ (where ζ is a cell–substrate friction coefficient dependent on cell–substrate adhesion and $\mathbf{v}_i = \partial_t \mathbf{r}_i$ the velocity of the cell vertex \mathbf{r}_i).

At the continuum limit and at linear order, force balance in such a monolayer reads

$$\tau_r \partial_t r(x, t) = \partial_{xx} r(x, t) - \partial_x l_0(x, t) \quad (1)$$

with all units normalized by the average cell length, and r the vertex position at distance x and time t . The first two terms are classical for overdamped chains of oscillators, and represent resp. frictional forces and restoring forces from active cell tensions (with $\tau_r = \zeta/k$, the ratio of cell–substrate friction to cell stiffness, giving a timescale for the spatiotemporal diffusion of displacement \mathbf{r} , on length scales of cell size). The third term arises from the fact that each cell at position x can in principle have its own preferred length l_0 , so that gradients of preferred length result in cellular

flows. We find that long-term viscoelasticity arising, for instance, from rearrangements and occurring on timescales longer than the observed density oscillations¹⁵ does not have a strong effect on pattern formation and is safe to neglect for our analysis (Supplementary Section II E). We also neglect cellular proliferation, given experimental evidence that it is not required for wave formation¹⁵.

We now seek to couple this mechanical model to the internal chemical state of the cells. Given the reported impact of ERK activity on actomyosin^{14,25,27}, we assume generic couplings between ERK activity and all tensions $\gamma_{a,b,l}$ (ERK). Importantly, as each of these dependencies can be different, ERK activity is expected to generically modify the preferred length ($l_0 = l_0(\text{ERK})$, and thus the preferred cellular density), with a delay that we denote as τ_l . This is supported by recent evidence in MDCK monolayers, which showed that varying ERK activity causes relative changes in F-actin intensity and structure in the lateral and basal surfaces²⁷. Assuming linear, first-order kinetics, this effect can be described as

$$\tau_l \partial_t l_0(x, t) = l_0^{\text{eq}} - l_0(x, t) - \alpha(E(x, t) - E_{\text{eq}}) \quad (2)$$

where l_0^{eq} is the normal, ‘homeostatic’ rest length, which sets the length scale of the problem and corresponds to steady-state ERK activity E_{eq} , and α is the coefficient of coupling between ERK activity and preferred size. In principle α can have any sign, however optogenetic activation of ERK in MDCK monolayers causes cellular contraction²⁷, suggesting that $\alpha > 0$ in this system.

Finally, given the reported mechanosensitivity of ERK and its dependency on cell length ($\partial_x r$, inversely proportional to cell density)²⁷, a minimal equation for ERK activity, again assuming generic first-order couplings, reads

$$\tau_E \partial_t E(x, t) = E_{\text{eq}} - E(x, t) + \beta \partial_x r(x, t) \quad (3)$$

with the timescale τ_E indicating how quickly ERK reacts to mechanical deformations, and β determining the strength of coupling between cell length and ERK activity. Live measurements of ERK activity demonstrate that stretching MDCK monolayers results in an activation of ERK²⁷, suggesting that $\beta > 0$ in this system (see Supplementary Section II A for further details).

We now re-define variables $E = E - E_{\text{eq}}$ and $l_0 = l_0 - l_0^{\text{eq}}$ so that we only look at perturbations around steady state, and the full model reads

$$\begin{cases} \tau_r \partial_t r = \partial_{xx} r - \partial_x l_0 \\ \tau_l \partial_t l_0 = -l_0 - \alpha E \\ \tau_E \partial_t E = -E + \beta \partial_x r \end{cases} \quad (4)$$

We perform a linear stability analysis to test whether this minimal mechanochemical model reproduces the features of density and ERK patterns observed in epithelial monolayers. This yields the following dispersion relation for patterns of temporal frequency ω and spatial frequency q :

$$(\tau_E \omega + 1)(\tau_l \omega + 1)(\tau_r \omega + q^2) = -\alpha \beta q^2 \quad (5)$$

We see that there are only three independent quantities in this problem: two ratios of timescales (τ_E/τ_l and τ_r/τ_l), as well as the product of the two coupling coefficients $\alpha\beta$, which quantifies the global strength of the ERK–density mechanochemical feedback loop. Examining the evolution of the dispersion relation $\omega(q)$ reveals a critical threshold for $\alpha\beta$ above which an instability occurs (Supplementary Section I B), characterized by a finite length scale and non-zero imaginary frequency indicative of stable temporal oscillations (Fig. 1f). This means that complex

spatiotemporal patterns of ERK and density are expected to arise with length scale

$$\lambda_c = 2\pi \frac{\tau_E^{1/4} \tau_l^{1/4}}{\tau_r^{1/2}} \quad (6)$$

and temporal frequency

$$\omega_c^2 = \frac{1}{\tau_l^{1/2} \tau_E^{3/2}} + \frac{1}{\tau_l^{3/2} \tau_E^{1/2}} + \frac{1}{\tau_l \tau_E}, \quad (7)$$

which is confirmed in numerical simulations (Fig. 1g, Extended Data Fig. 2a,b, and see Extended Data Fig. 3 for detailed nonlinear analysis).

Since the frequency of the emergent oscillation depends only on the timescales τ_l and τ_E , we can infer that the instability arises from local activator–inhibitor dynamics between the preferred cellular length and ERK activity. The remaining timescale τ_r for the magnitude of substrate friction (that is, mechanical relaxation), determines how far local deformations propagate over one period of oscillation, which explains the finite length scale of the instability. This minimal model requires only scalar active terms^{20,39} to produce patterns of density, velocity and ERK activity at finite length and time scales, without the need for active polar forces^{14–17}. We also note that density waves are abolished by inhibition¹⁴, but also by overactivation of ERK (Extended Data Fig. 1), which is in full agreement with the predictions of our model (Extended Data Fig. 2c). These findings show that ERK oscillations are not merely a byproduct of an upstream density oscillation (as observed for yes-associated protein (YAP) oscillations¹⁶), but rather a core element of the dynamics, and thus amenable to experimental perturbations.

Indeed, equations (6) and (7) make further quantitative predictions that depend only on macroscopic parameters, that is, the three timescales τ_r , τ_E and τ_l (see Extended Data Figs. 2–4 for sensitivity analysis), which we now seek to infer from mechanical stretching and optogenetic activation experiments in MDCK monolayers²⁷. Firstly, mechanical stretching accompanied by live reporting of ERK activity (Fig. 2a) offers the ideal platform to measure τ_E since it is the timescale of ERK activation post-stretch. Comparing equation (3) to the data of ref.²⁷ reveals good fits (Fig. 2b and Extended Data Fig. 5a), which validates our hypothesis of first-order kinetics and dependency of ERK activity on cell density, and allows us to infer $\tau_E = 4–8$ min (we also took into account longer-term desensitization of ERK, although this has little impact on the results, see Supplementary Section II A and Extended Data Fig. 4). Secondly, optogenetic activation of ERK and observation of subsequent cellular contraction²⁷ (Fig. 2c) provides a dataset from which to infer τ_r and τ_l , as well as an opportunity to validate the mechanical model (equations (1) and (2)) for externally imposed ERK dynamics. When a step function in ERK activation is applied, the model predicts cellular shrinking at timescale τ_l beginning at the boundary between high and low ERK activity, where forces are unbalanced, and diffusing into the monolayer at timescale τ_r (see section ‘Parameter estimation’ in the Methods). We thus tracked cells to follow the spatiotemporal dynamics of monolayer contraction $r(x, t)$ (raw data from ref.²⁷). Fitting this dataset to our analytical prediction (equation (18)) reveals qualitative and quantitative agreement, which allows us to infer $\tau_l = 100–140$ min and $\tau_r = 5–16$ min (Fig. 2d–f, Extended Data Fig. 5b–d and see Extended Data Fig. 6 for details). Strikingly, these estimates predict a typical length scale λ_c and temporal period T_c of density and ERK patterns at the onset of instability

$$\lambda_c = 7 – 16 \text{ cell diameters} ; T_c = 50 – 90 \text{ min}, \quad (8)$$

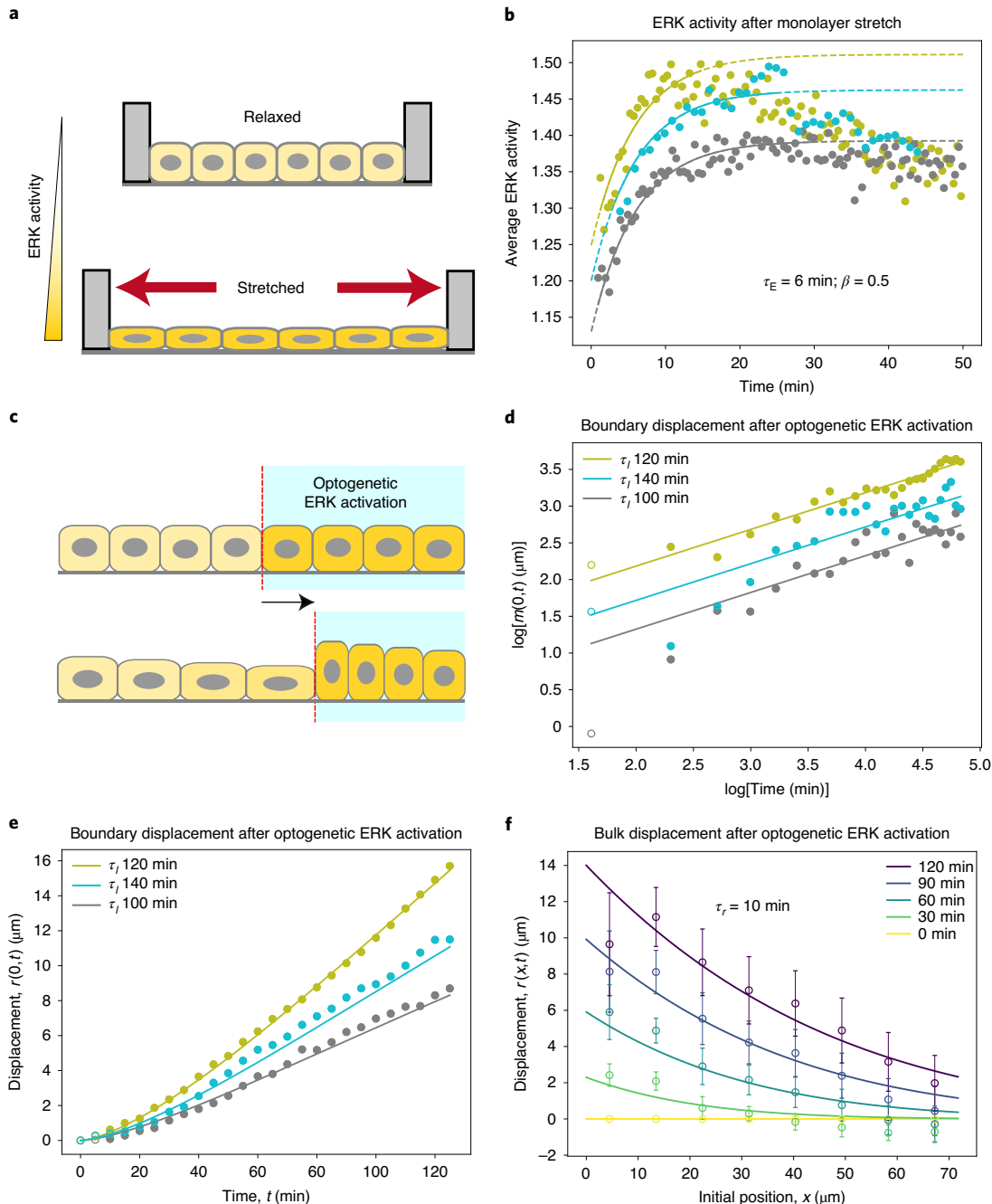


Fig. 2 | Parameter fitting using mechanical and optogenetic perturbation experiments. **a**, Response of ERK activity to a 50% uniaxial stretch ($N = 3$, from ref. ²⁷). **b**, Equation (3) provides a good fit for the data (dots, each colour shows an independent experiment), from which we extract $\tau_E = 4–8 \text{ min}$ and $\beta = 0.5–0.6$ (best fit values shown in panel). Solid lines indicate the model fits. **c**, Optogenetic activation of ERK in a patch of cells causes cellular contraction from the boundary ($N = 3$, from ref. ²⁷). **d–f**, Our model provides a good fit for the displacement of the boundary during contraction (**d,e**: each colour shows an independent experiment) as well as the full spatiotemporal evolution of the cell displacement field $\mathbf{r}(x, t)$ (**f**) upon ERK activation at $t = 0$ (see section ‘Parameter estimation’ in the Methods), allowing us to extract $\tau_I = 100–140 \text{ min}$ and $\tau_r = 5–16 \text{ min}$ (best fit value shown in panel). Error bars in **f** show the standard error around the mean taken from the three repeats.

which describes well, and in a parameter-free manner, the dynamics observed experimentally both in confluent and migrating MDCK layers (Fig. 1a–d, Extended Data Fig. 1a,b and Supplementary Video 1). Furthermore, the model predicts ERK waves to trail behind density waves by a characteristic timescale of τ_E , in agreement with our data (3–5 min from Fig. 1d).

Although our proposed mechanism is sufficient to explain isotropic patterns in confluent tissues, we still need to explain how symmetry is broken to allow for unidirectional waves and long-range

cell polarity in migrating monolayers with a free boundary (Fig. 3a)²⁷. For this, we couple our model to cell polarity \mathbf{p} (sketched in Fig. 3b), a continuous variable taking both positive and negative values. This adds an active polar traction force to equation (1) (in addition to the previous cell–substrate friction force $\tau_s \partial_x \mathbf{r}$), corresponding to cells exerting forces on the substrate in the direction opposite to \mathbf{p} . In MDCK cells, polar traction forces are generated by polarized lamellipodia^{15,40}. It has been reported, in particular, that cells polarize in response to tension transmitted through cell–cell

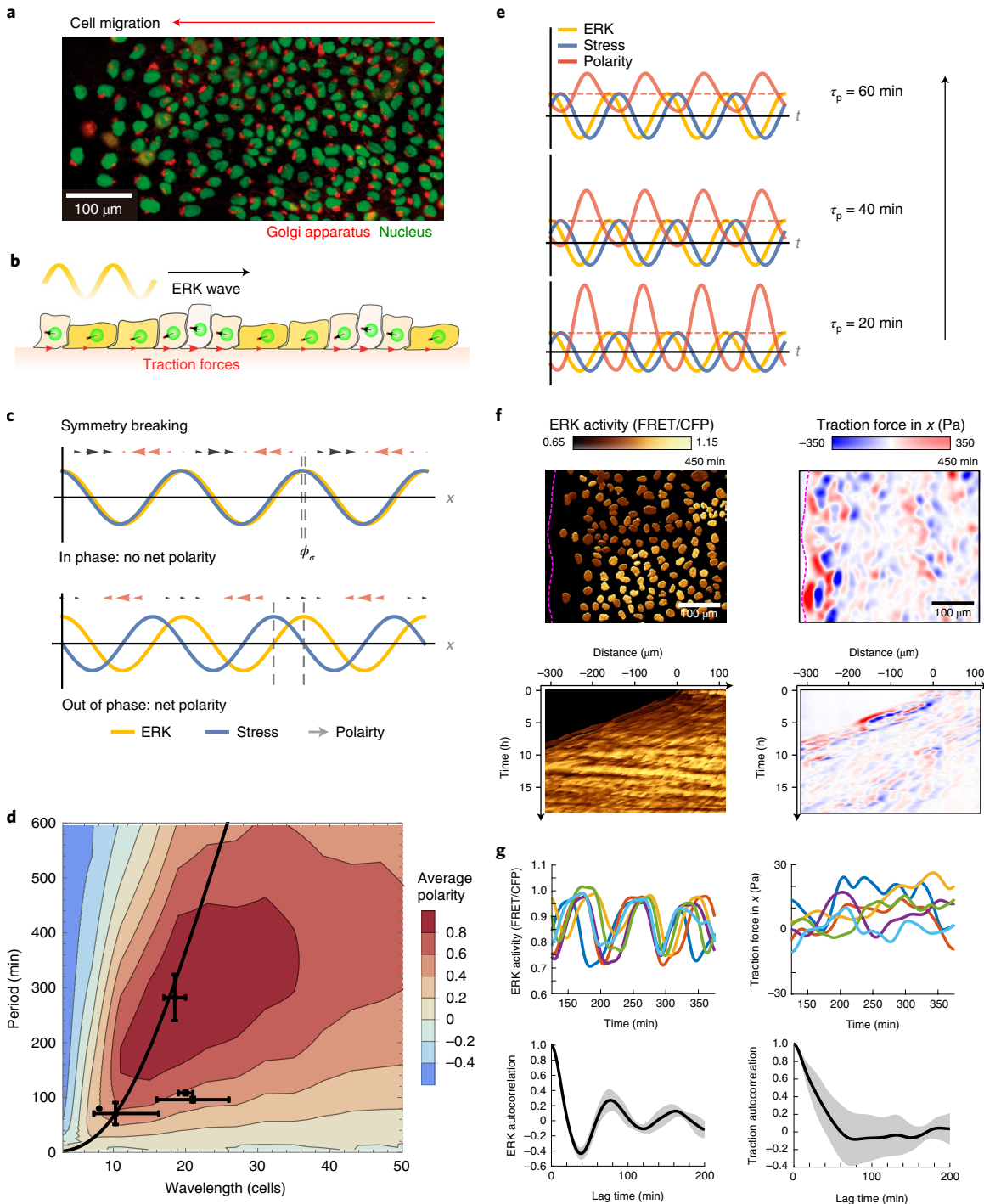


Fig. 3 | Response of active polar traction forces to an applied ERK wave and comparison with traction force data. **a**, Migrating MDCK monolayers polarize towards a free edge as visualized by the orientation of the Golgi apparatus (red) relative to the nucleus (green) (see ref. ²⁷). **b**, Schematic of our mechanochemical model extended to include cell polarization and active migration. **c**, If polarity follows gradients of stresses, monolayers can exploit phase differences (ϕ_σ) between ERK and stress to produce net polarization from symmetric waves. **d**, Quantitative phase diagram of the average cell polarity in response to applied ERK waves, showing an optimal period and wavelength for inducing maximal average polarity (positive values in red indicate polarity counter to ERK waves). Data points are previously reported values for wavelength and period in MDCK layers ^{17,25,27} and mouse skin ²⁶ (see Supplementary Section IC for details). Importantly, the waves permissible by our biophysical model (black curve for varying τ_p) produce only positive average polarity, thus providing robustness to the migration response. **e**, Oscillations in polarity and traction forces are weakened for longer timescales of polarization τ_p whereas their average (dashed line) is unaffected. **f**, ERK activity and corresponding traction forces measured in an expanding monolayer. Dashed lines indicate the leading edge of the monolayer. Kymographs show that the intercellular wave propagation present in ERK activity is absent in traction forces. **g**, Single-cell traces (six representative cells, colour-coded) of ERK activity show a strong oscillatory component (autocorrelation function), whereas corresponding local traction forces show a much weaker oscillatory component (as predicted in **e**). Shaded areas, standard deviation.

junctions^{6,15,40,41}, so that the simplest equation for polar orientation reads $\tau_p \partial_t p = -p - \gamma \partial_x \sigma_{xx}$, where τ_p is a timescale of relaxation and $\gamma > 0$ is a coupling strength between polarity and gradients of cellular stresses, $\partial_x \sigma_{xx} = \partial_x (\partial_x r - l_0)$ (see Supplementary Section II D for a discussion of alternative couplings, for example to velocity¹⁸).

Before studying the fully coupled system, we first explore the limiting case of externally driven ERK dynamics (Fig. 3b). Although the couplings in our model allow ERK waves to translate into changes in polarity, a solely linear theory cannot break symmetry to produce unidirectional polarization. This is similar to the ‘back-of-the-wave’ paradox encountered in the collective migration of *Dictyostelium* from diffusible chemical waves^{42,43}. However, we reasoned that nonlinearities (combined with phase differences between ERK and mechanics) can allow for symmetry breaking, for instance if the stress–polarity coupling is modulated by ERK activity ($\gamma = \gamma(\text{ERK})$). This is consistent with recent experiments where ERK activation (resp. inhibition) was shown to decrease (resp. increase) mean traction forces in MDCK layers²⁷, implying, moreover, that γ is a decreasing function of ERK activity (see Supplementary Section II F and Extended Data Fig. 7 for discussion and exclusion of alternative forms of nonlinearity). This could provide a generic mechanism to take advantage of phase differences between ERK activity and mechanical stress, to allow cells to be largely insensitive to the positive gradients of approaching mechanical waves, while responding strongly to the negative gradient of the receding part (see Fig. 3c for a sketch). When we analyse this we find that a maximum global polarization occurs when stress lags ERK by $\pi/4$, which occurs only at a single optimum of the wavelength λ and temporal period T of the applied ERK wave (Fig. 3d and Supplementary Section I C). Since stress $\sigma = \partial_x r - l_0$ involves the hidden variable l_0 it is more convenient to consider the delay to cell length $l = \partial_x r$ that is predicted to precede ERK activity by a phase of $\pi/4$ at optimum. This agrees qualitatively with the delay observed in data (Fig. 1d).

Using the timescales inferred above allows us to predict the values of this optimum (Fig. 3d), which we find to be $\lambda \approx 10\text{--}35$ cells and $T \approx 2\text{--}7$ h (see simulations of the full model with ERK desensitization, or slightly longer without, Supplementary Section II A and Extended Data Fig. 8). Strikingly, this is close to the natural waves observed both in MDCK layers ($\lambda \approx 20$ cells, $T \approx 1$ h in our data and refs. ^{25,27}, $\lambda \approx 20$ cells, $T \approx 4.7$ h in ref. ¹⁷) and mouse skin ($\lambda \approx 8$ cells and $T \approx 1.3$ h in ref. ²⁶), suggesting that these systems might be tuned for optimal migration. This is also in agreement with optogenetic experiments that applied waves of a given wavelength, but varying speed (that is, period), to MDCK monolayers, demonstrating the existence of an optimal wave speed for inducing cell movement²⁵ ($\approx 2 \mu\text{m min}^{-1}$ in both data and our model). Furthermore, although any wave characteristic is possible in optogenetic experiments, the mechanism for spontaneous pattern formation that we described above permits only waves that translate into net polarization in the direction opposite to the propagation of ERK (Fig. 3d). In other words, the system robustly directs migration counter to ERK waves for any model parameters.

We also investigated how polarity is predicted to evolve spatiotemporally in response to an applied ERK wave (Supplementary equation (20)). Although the average polarity shown in Fig. 3d is independent of the polarization relaxation timescale τ_p , the amplitude of polarity oscillations around the average depends critically on it, with longer values dampening the amplitude of the oscillations (Fig. 3e). Interestingly, experimentally measured values ($\tau_p \approx 15\text{--}40$ min; refs. ^{15,27,40,41}) were sufficient to abolish negative contributions to polarity in response to an applied wave. This provides an explanation for the seemingly paradoxical observation that supracellular polar traction forces during collective cell migration display near-constant long-ranged order²⁷ despite the presence of spatiotemporal oscillations in stress¹¹. To further test whether this is also the case for the long-range orientation of traction forces, we measured traction force profiles in a migrating

monolayer together with ERK activity, and confirmed that oscillations in traction forces are weak compared with the strongly periodic ERK oscillations (Fig. 3f,g and Supplementary Video 2).

Next, we explored the full interplay between mechanochemical ERK patterns and active migration forces, which is the typical scenario of monolayer expansion in the presence of free boundaries. Simulations in one dimension consisted of Supplementary equation (14), supplemented with boundary conditions at the free edge (specifically $\mathbf{p} = \mathbf{p}_b$ to model the presence of leader cells^{7,11}, see section ‘Numerical simulation’ in the Methods). We found that simulations in the presence of bulk polarity displayed ERK waves robustly propagating backwards from the free edge (Fig. 4a), which gradually polarized cells in bulk, leading to long-range polar order (Extended Data Fig. 9a) (as in the response to a driven ERK wave). This recapitulated well the experimentally observed dynamics (Fig. 4a and ref. ²⁷). Conversely, for strong leader cells and comparatively low bulk polarity, the model predicts waves in the reverse direction (centre to edge) (Extended Data Fig. 9c), suggesting a key role for stress–polarity coupling in determining wave directionality.

Although multiple experimental set-ups produce density waves propagating backward from the edge^{15,27}, some groups report more complex dynamics such as a front of uniformly high ERK activity propagating from the boundary^{25,34}. Interestingly, our model predicts this behaviour for cell monolayers cultured at initially higher density (uniform cell length smaller than the preferred length, that is, $l < l_0$, as initial condition), where the first stages of expansion are dominated by mechanical relaxation (as reported in ref. ⁴⁴) that triggers a low density (that is, high ERK) front propagating away from the boundary. To test this prediction we cultured cells at higher density before release, and found good qualitative agreement (Fig. 4b and Supplementary Video 3), arguing that cellular density could explain the different ERK dynamics observed in previous experiments^{25,27}.

Finally, we sought to test the key model prediction that stress–polarity couplings are not the origin of mechanochemical waves, but rather cause symmetry breaking (that is, unidirectional wave propagation in response to a free edge) of existing mechanochemical patterns. For this, we examined ERK dynamics in Merlin knockout cells, as Merlin has been shown to be a key link between cell–cell-mediated force transmission and Rac1-driven polarized lamellipodia formation in MDCK monolayers⁴⁰. We thus expect the coupling coefficient γ to be drastically reduced in this condition ($\gamma \approx 0$). Strikingly, Merlin knockout monolayers still displayed prominent ERK waves, with wavelength and time period indistinguishable from controls (Extended Data Fig. 9d and Supplementary Video 4), but with loss of directional ERK wave propagation (Fig. 4c and Extended Data Fig. 9b), in agreement with the model.

Discussion

Altogether, we provide a theoretical framework for the emergence of complex mechanochemical patterns and long-ranged coordinated migration in MDCK monolayers. We show that spatiotemporal waves of cellular density and ERK activity arise from a scalar active matter instability caused by delayed mutual feedbacks between tissue mechanics and mechanosensitive ERK activity²⁷. Quantifying datasets from optogenetic and mechanical perturbation experiments²⁷, we tested the model and extracted the key timescales of the system, providing parameter-free predictions for the appearance, wavelength and period of ERK (and density) patterns, which fits well with previously published data, as well as our own. Our results suggest that interplays between stresses and migratory forces are not the driver of the instability itself, but are instead required to orient ERK (and density) waves unidirectionally and establish long-range polar order. Remarkably, we show that this mechanism robustly induces polarization in a preferred direction and that biophysical parameters are tuned for a close to optimal migration response, that is, the wavelength and period of the observed waves are close to

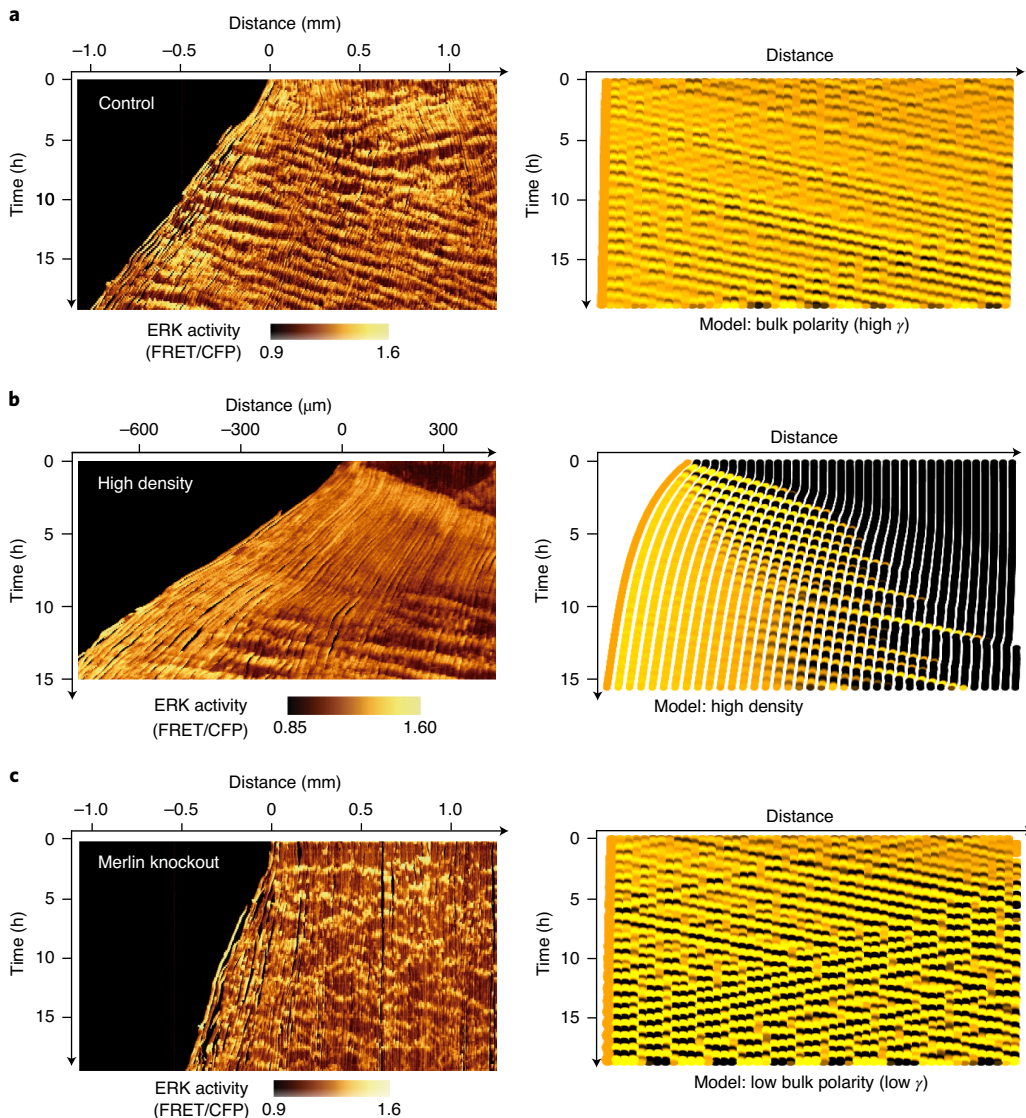


Fig. 4 | The model predicts the spatiotemporal dynamics of expanding monolayers in a variety of experimental settings. **a**, Using the parameters fitted above, together with a boundary condition of leader cells (see section ‘Numerical simulation’ in the Methods), the model (right) reproduces the transition from initially random to unidirectional ERK wave propagation seen in the data for expanding monolayers (left). **b**, The model also reproduces the effect of increasing cell density, with initially low ERK activity everywhere in the monolayer, followed by a ‘tidal’ wave²⁵ of ERK activity (which remains high in the front as waves start appearing in the back). **c**, Merlin knockouts (left) designed to inhibit polarization via cell-to-cell tension⁴⁰. ERK waves are still present but become randomly orientated, matching the model predicted for weaker stress–polarity coupling ($\gamma \approx 0$, right).

the theoretical optimum for inducing maximal average polarization and active migration in the direction of free edges.

Our theory thus provides a bridge between the biophysical origin of spatiotemporal patterns and the design principles underlying collective cell migration, with ERK playing a central role of integrating chemical and mechanical signals. Cell–cell mechanical coupling (which is required for waves to occur in MDCK²⁷ monolayers), together with cell–substrate friction, results in spatial diffusion of mechanical stress, which can act as a relay mechanism to (1) modulate cellular density (and ERK) activity and (2) orient cell polarity (and traction forces) (in conjunction with ERK itself). This biological mechanism contrasts with a similar phenomenon in *Dictyostelium* where waves and symmetry breaking rely on extracellular chemical diffusion^{42,43}, although exploring systematically the potential conceptual and mathematical connection between both mechanisms would be an interesting next step. Moreover, integrating details of known biochemical networks and more complex

mechanical properties of tissues⁴⁶ could enrich the dynamics of our model even further. Candidates for inclusion include RhoGTPases⁴⁵ (which can form feedback loops with myosin^{47,48}) or mechanotransduction at the level of adherens junctions⁴⁹ and adherens junctions (which features crosstalks with ERK⁵⁰). Understanding better the role of nonlinearities and temporal adaptation in these pathways will also be key to deciphering their function.

There are also other patterning phenomena for which we could test and extend our theoretical model. For instance, tissue-scale mechanochemical waves have been observed to drive morphogenesis in multiple developmental settings, such as tracheal⁵¹ and endoderm⁴⁸ morphogenesis in *Drosophila*. In the former case, waves arise from a positive biochemical feedback loop from EGFR–ERK signalling between neighbouring cells (EGFR, epidermal growth factor receptor), leading to a relay mechanism and wave propagation that translates to a wave of myosin II cable formation. In the latter case, wave propagation relies on a mechanosensitive feedback

where myosin II-generated stresses in a cell activate myosin II in the neighbour. Cellular-level temporal oscillations in the area of *Drosophila* amnioserosa cells have also been proposed to arise via a theory integrating tensile stresses and myosin activity³⁹.

Beyond biophysical mechanisms relating to pattern formation, the downstream effects (for example on collective cellular invasion in cancer or stem cell proliferation/differentiation) of multiple signalling pathways have been shown to depend not only on average biochemical levels, but also on their spatiotemporal dynamics^{30,52,53}. This begs the more general question of how spatiotemporal patterns are translated into robust cellular responses in different settings. Considering together the biophysical origin and design principles underlying these behaviours could provide a useful strategy for furthering our understanding of these processes.

Online content

Any methods, additional references, Nature Research reporting summaries, source data, extended data, supplementary information, acknowledgements, peer review information; details of author contributions and competing interests; and statements of data and code availability are available at <https://doi.org/10.1038/s41567-020-01037-7>.

Received: 26 February 2020; Accepted: 11 August 2020;

Published online: 28 September 2020

References

- Friedl, P. & Gilmour, D. Collective cell migration in morphogenesis, regeneration and cancer. *Nat. Rev. Mol. Cell Biol.* **10**, 445–457 (2009).
- Aragona, M. et al. Defining stem cell dynamics and migration during wound healing in mouse skin epidermis. *Nat. Commun.* **8**, 14684 (2017).
- Park, S. et al. Tissue-scale coordination of cellular behaviour promotes epidermal wound repair in live mice. *Nat. Cell Biol.* **19**, 155–163 (2017).
- Krndija, D. et al. Active cell migration is critical for steady-state epithelial turnover in the gut. *Science* **365**, 705–710 (2019).
- Marchetti, M. C. et al. Hydrodynamics of soft active matter. *Rev. Mod. Phys.* **85**, 1143–1189 (2013).
- Alert, R. & Trepat, X. Physical models of collective cell migration. *Annu. Rev. Condens. Matter Phys.* **11**, 77–101 (2020).
- Poujade, M. et al. Collective migration of an epithelial monolayer in response to model wound. *Proc. Natl Acad. Sci. USA* **104**, 15988–15993 (2007).
- Trepat, X. et al. Physical forces during collective cell migration. *Nat. Phys.* **5**, 426–430 (2009).
- Angelini, T. E. et al. Glass-like dynamics of collective cell migration. *Proc. Natl Acad. Sci. USA* **108**, 4714–4719 (2011).
- Blanch-Mercader, C. et al. Turbulent dynamics of epithelial cell cultures. *Phys. Rev. Lett.* **120**, 208101 (2018).
- Serra-Picamal, X. et al. Mechanical waves during tissue expansion. *Nat. Phys.* **8**, 628–634 (2012).
- Zaritsky, A. et al. Propagating waves of directionality and coordination orchestrate collective cell migration. *PLoS Comput. Biol.* **10**, e1003747 (2014).
- Rodriguez-Franco, P. et al. Long-lived force patterns and deformation waves at repulsive epithelial boundaries. *Nat. Mater.* **16**, 1029–1037 (2017).
- Notbohm, J. et al. Cellular contraction and polarization drive collective cellular motion. *Biophys. J.* **110**, 2729–2738 (2016).
- Tlili, S. et al. Collective cell migration without proliferation: density determines cell velocity and wave velocity. *R. Soc. Open Sci.* **5**, 172421 (2018).
- Peyret, G. et al. Sustained oscillations of epithelial cell sheets. *Biophys. J.* **117**, 464–478 (2019).
- Petrolli, V. et al. Confinement-induced transition between wavelike collective cell migration modes. *Phys. Rev. Lett.* **122**, 168101 (2019).
- Basan, M., Elgeti, J., Hannezo, E., Rappel, W. J. & Levine, H. Alignment of cellular motility forces with tissue flow as a mechanism for efficient wound healing. *Proc. Natl Acad. Sci. USA* **110**, 2452–2459 (2013).
- Garcia, S. et al. Physics of active jamming during collective cellular motion in a monolayer. *Proc. Natl Acad. Sci. USA* **112**, 15314–15319 (2015).
- Banerjee, S., Utujo, K. J. & Marchetti, M. C. Propagating stress waves during epithelial expansion. *Phys. Rev. Lett.* **114**, 228101 (2015).
- Yabunaka, S. & Marcq, P. Emergence of epithelial cell density waves. *Soft Matter* **13**, 7046–7052 (2017).
- Blanch-Mercader, C. & Casademunt, J. Hydrodynamic instabilities, waves and turbulence in spreading epithelia. *Soft Matter* **13**, 6913–6928 (2017).
- Harvey, C. D. et al. A genetically encoded fluorescent sensor of ERK activity. *Proc. Natl Acad. Sci. USA* **105**, 19264–19269 (2008).
- Komatsu, N. et al. Development of an optimized backbone of FRET biosensors for kinases and GTPases. *Mol. Biol. Cell* **22**, 4647–4656 (2011).
- Aoki, K. et al. Propagating wave of ERK activation orients collective cell migration. *Dev. Cell* **43**, 305–317 (2017).
- Hiratsuka, T. et al. Intercellular propagation of extracellular signal-regulated kinase activation revealed by *in vivo* imaging of mouse skin. *eLife* **4**, e05178 (2015).
- Hino, N. et al. ERK-mediated mechanochemical waves direct collective cell polarization. *Dev. Cell* **53**, 646–660 (2020).
- de la Cova, C., Townley, R., Regot, S. & Greenwald, I. A real-time biosensor for ERK activity reveals signaling dynamics during *C. elegans* cell fate specification. *Dev. Cell* **42**, 542–553 (2017).
- Moreno, E., Valon, L., Levillayer, F. & Levayer, R. Competition for space induces cell elimination through compaction-driven ERK downregulation. *Curr. Biol.* **29**, 23–34 (2019).
- Johnson, H. E. et al. The spatiotemporal limits of developmental Erk signaling. *Dev. Cell* **40**, 185–192 (2017).
- Howard, J., Grill, S. W. & Bois, J. S. Turing's next steps: the mechanochemical basis of morphogenesis. *Nat. Rev. Mol. Cell Biol.* **12**, 392–398 (2011).
- Hannezo, E. & Heisenberg, C. P. Mechanochemical feedback loops in development and disease. *Cell* **178**, 12–25 (2019).
- Szabo, B. et al. Phase transition in the collective migration of tissue cells: experiment and model. *Phys. Rev. E* **74**, 061908 (2006).
- Matsubayashi, Y., Ebisuya, M., Honjoh, S. & Nishida, E. ERK activation propagates in epithelial cell sheets and regulates their migration during wound healing. *Curr. Biol.* **14**, 731–735 (2004).
- Hannezo, E., Prost, J. & Joanny, J. F. Theory of epithelial sheet morphology in three dimensions. *Proc. Natl Acad. Sci. USA* **111**, 27–32 (2014).
- Alt, S., Ganguly, P. & Salbreux, G. Vertex models: from cell mechanics to tissue morphogenesis. *Phil. Trans. R. Soc. B* **372**, 20150520 (2017).
- Fouchard, J. et al. Curling of epithelial monolayers reveals coupling between active bending and tissue tension. *Proc. Natl Acad. Sci. USA* **117**, 9377–9383 (2020).
- Heisenberg, C. P. & Bellaïche, Y. Forces in tissue morphogenesis and patterning. *Cell* **153**, 948–962 (2013).
- Lin, S. Z., Li, B., Lan, G. & Feng, X. Q. Activation and synchronization of the oscillatory morphodynamics in multicellular monolayer. *Proc. Natl Acad. Sci. USA* **114**, 8157–8162 (2017).
- Das, T. et al. A molecular mechanotransduction pathway regulates collective migration of epithelial cells. *Nat. Cell Biol.* **17**, 276–287 (2015).
- Weber, G. F., Bjerke, M. A. & DeSimone, D. W. A mechanoresponsive cadherin-keratin complex directs polarized protrusive behavior and collective cell migration. *Dev. Cell* **22**, 104–115 (2012).
- Nakajima, A., Ishihara, S., Imoto, D. & Sawai, S. Rectified directional sensing in long-range cell migration. *Nat. Commun.* **5**, 5367 (2014).
- Xiong, Y., Huang, C. H., Iglesias, P. A. & Devreotes, P. N. Cells navigate with a local-excitation, global-inhibition-biased excitable network. *Proc. Natl Acad. Sci. USA* **107**, 17079–17086 (2010).
- Anon, E. et al. Cell crawling mediates collective cell migration to close undamaged epithelial gaps. *Proc. Natl Acad. Sci. USA* **109**, 10891–10896 (2012).
- Bui, J., Conway, D. E., Heise, R. L. & Weinberg, S. H. Mechanochemical coupling and junctional forces during collective cell migration. *Biophys. J.* **117**, 170–183 (2019).
- Recho, P., Hallou, A. & Hannezo, E. Theory of mechanochemical patterning in biphasic biological tissues. *Proc. Natl Acad. Sci. USA* **116**, 5344–5349 (2019).
- Qin, X. et al. A biochemical network controlling basal myosin oscillation. *Nat. Commun.* **9**, 1210 (2018).
- Bailles, A. et al. Genetic induction and mechanochemical propagation of a morphogenetic wave. *Nature* **572**, 467–473 (2019).
- Pinheiro, D. & Bellaïche, Y. Mechanical force-driven adherens junction remodeling and epithelial dynamics. *Dev. Cell* **47**, 3–19 (2018).
- Hamouda, M. S., Labouesse, C. & Chalut, K. J. Nuclear mechanotransduction in stem cells. *Curr. Opin. Cell Biol.* **64**, 97–104 (2020).
- Ogura, Y., Wen, F. L., Sami, M. M., Shibata, T. & Hayashi, S. A switch-like activation relay of EGFR-ERK signaling regulates a wave of cellular contractility for epithelial invagination. *Dev. Cell* **46**, 162–172 (2018).
- Aoki, K. et al. Stochastic ERK activation induced by noise and cell-to-cell propagation regulates cell density-dependent proliferation. *Mol. Cell* **52**, 529–540 (2013).
- Isomura, A. & Kageyama, R. Ultradian oscillations and pulses: coordinating cellular responses and cell fate decisions. *Development* **141**, 3627–3636 (2014).

Publisher's note Springer Nature remains neutral with regard to jurisdictional claims in published maps and institutional affiliations.

© The Author(s), under exclusive licence to Springer Nature Limited 2020

Methods

Cell culture. MDCK cells (no. RCB0995, RIKEN BioResource Center) were used for this study. The experiments were performed with a culture medium including Medium 199 (no. 11043-023; ThermoFisher Scientific), 10% fetal bovine serum (no. 172012-500ML, Sigma-Aldrich), 100 unit ml⁻¹ penicillin and 100 µg ml⁻¹ streptomycin (no. 26253-84, Nacalai Tesque). Further details are described elsewhere²⁷.

CRISPR–Cas9-mediated knockout of Merlin. LentiCRISPRv2-bleo was constructed by replacing the puromycin resistance gene in lentiCRISPRv2 (Addgene Plasmid: no. 52961) with the bleomycin resistance gene. For CRISPR–Cas9-mediated knockout of dog *Nf2* (Merlin), two single guide RNAs (sgRNA) targeting the exons of NF2 were designed using CRISPRdirect³⁴. The following sequences were used for the sgRNA sequences: CCTGGCTTACGCCGTCC (sgRNA1) and GACCCTCTGTTACAAACG (sgRNA2). DNA oligonucleotides for the sgRNA1 and sgRNA2 were cloned into the lentiCRISPRv2 and lentiCRISPRv2-bleo vectors, respectively. To increase the knockout efficiency, the sgRNA1 and sgRNA2 together with Cas9 were simultaneously introduced into MDCK cells by the lentivirus. The infected cells were selected with 2 µg ml⁻¹ puromycin and 100 µg ml⁻¹ zeocin. After selection, the reduction in the expression levels of the proteins was confirmed by immunoblotting. Bulk cells were used for the experiments.

Migration and confluence assay. A culture insert with 2 wells (no. 81176, ibidi GmbH) was placed on a glass-based dish (no. 3911-035, AGC Techno Glass) pre-coated with 0.3 mg ml⁻¹ type I collagen (Nitta Gelatin). MDCK cells (7×10^3 cells) expressing the plasmid EKAREV-NLS²⁴ were seeded in each well of the culture insert. For the migration assay, the culture insert was removed 24 h after seeding. For the migration assay with high density, cells were cultured for a longer period of 48 h prior to release to increase the cell number. For confluence assays, the imaging was performed 24 h after seeding without removing the culture insert. The cells were imaged with an epifluorescence microscope every 1 to 10 min, starting 30 min after the removal of the culture insert.

Time-lapse imaging. The details of the time-lapse FRET imaging conditions are described in ref.²⁷. Briefly, cells were imaged with an IX83 inverted microscope (Olympus) equipped with a UPlanFL-PH 10×/0.3 (Olympus) or a UPlanSApo 40×/0.95 objective lens (Olympus), a DOC CAM-HR CCD camera (Molecular Devices), and a stage top incubator (Tokai Hit). The filters and dichromatic mirrors used for time-lapse imaging were: a 438/24 excitation filter, a FF458-Di02-25×36 dichromatic mirror, and FF01-483/32-25 and FF01-542/27-25 emission filters (Semrock) for cyan fluorescent protein (CFP) and FRET, respectively.

Cell stretching. MDCK cells (2×10^5 cells) were seeded on an elastic silicone chamber (no. STB-CH-04, STREX) pre-coated with 0.3 mg ml⁻¹ type I collagen (Nitta Gelatin). After 24 h incubation, the MDCK cells on the stretch chamber were uniaxially stretched by 50% with a manual cell-stretching system (no. STB-100-04, STREX) on an epifluorescence microscope.

Optogenetic ERK activation. The optogenetic ERK activation experiment using the CRY2-CIBN system is described elsewhere²⁷. Briefly, MDCK cells in which ERK is activated in response to blue light were seeded on one side of the two wells of a culture insert placed on a dish, and the non-light-responsive MDCK cells were seeded in the other well of the culture insert as well as outside the insert. Removal of the insert followed by incubation allowed the cells to fill the gap between the cell populations. The interface between the cell populations was imaged, and the cells were exposed to 438 nm blue LED light every 5 min to maintain ERK activation.

Traction force microscopy. Details of the traction force microscopy experiment are described elsewhere^{5,13,27}. Deep red fluorescent carboxylate-modified beads at a concentration of 0.01% (0.2 µm diameter; no. F8810, ThermoFisher Scientific) in phosphate-buffered saline (PBS) were included in 9 kPa gels (7.5% acrylamide, 0.1% bisacrylamide, 0.05% ammonium persulfate, 0.05% *N,N,N',N'*-tetramethyl ethylenediamine). Eighteen microlitres of the solution was dropped on the dishes and 18 mm glass coverslips were placed on top of them. After polymerization, the gels were covered with 2 mg ml⁻¹ sulfo-SANPAH, (a heterobifunctional crosslinker; no. ab145610, Abcam), and activated by ultraviolet light twice for 5 min and 7 min. The gels were coated with 100 µm ml⁻¹ type I collagen (Nitta Gelatin) overnight at 4 °C. Then, the gels were washed three times with PBS and incubated with culture medium for 1 h. For imaging, the bead fluorescence was obtained with an IX83 inverted microscope equipped with a 632/22 excitation filter, a glass dichromatic mirror (Olympus) and a FF01-692/40-25 (Semrock) emission filter. A reference image was obtained after the removal of cells by trypsinization. Traction forces were computed by Fourier-transform traction microscopy as described previously⁸.

Calculation of *x*-strain rate. The *x*-strain rate analysis is described in detail in ref.²⁷. Briefly, particle image velocimetry (PIV) was applied to phase contrast time-lapse images to calculate the velocity fields of cells. We defined the *x*-strain

rate as the spatial derivative of the velocity field along the *x* axis (migration axis) divided by the distance between the centres of two adjacent interrogation windows of the PIV analysis. The obtained discrete data assigned to each interrogation window were processed by a cubic interpolation method to fill the gap.

Quantification of ERK activity and traction force. To represent the FRET efficiency, FRET/CFP ratio images were generated after the background intensity was subtracted from the original fluorescence images in the CFP and FRET channels, respectively, using Metamorph (Molecular Devices) or MATLAB (Mathworks). Then, the Fiji TrackMate plugin was applied to the CFP fluorescence images for tracking each cell. The obtained time-series data of ERK activation were processed with a Savitzky–Golay filter to reduce the noise.

Statistical tests. Statistical tests, sample sizes, test statistics and *P* values are described in the figure legends. No statistical analysis was used to predetermine the sample size. *P* values of less than 0.05 were considered to be statistically significant in two-tailed tests.

Cross-correlation analysis. To obtain ERK and cell area data for cross-correlation we tracked cell centres and ERK activity as described above, and performed a Voronoi tessellation to infer the corresponding cell areas. This allowed us to build a dataset of joint temporal traces for ERK activity and cell area. We excluded all cells at tessellation borders since their areas could not be determined. If the change in cell area between two consecutive time steps was larger than 10%, we assigned a new cell ID to the latter time trace and considered it as a new trace (as this change was likely to be caused by a local cell division whose effects we wished to exclude). We also excluded all cells with a time trace shorter than 10 time steps.

We calculated the cross-correlation between cell area and ERK activity (as shown in Fig. 1) using the definition

$$(E * A)(\tau) = \frac{1}{\sigma_E \sigma_A} \sum_{i=1}^N E(t_i + \tau)A(t_i) \quad (9)$$

such that positive τ corresponds to ERK activity following cell area, with normalization using σ_E and σ_A , the independent standard deviations of the ERK activation and area signals. Each trace was $N = 20$ time steps (100 min) long and mean-subtracted across both cells and time. Cross-correlations were averaged over three repeats of the confluent phase to obtain the means and standard deviations plotted in Fig. 1d, with at least 7,540 cells averaged within each repeat. We note that the absolute value of the maximal cross-correlation is not very instructive here, as it can be lowered artificially by extrinsic measurement noise such as segmentation and tracking errors. However, the delay in the peak of cross-correlation can be used, and is consistent with our model and mechanical stretching experiments, predicting a small temporal delay between area and ERK activity. The autocorrelations in Fig. 3g were calculated according to the same formula using six representative cells (from those with smooth temporal profiles of ERK activity and trackable for more than 3 h) to compare autocorrelation of ERK activity and traction forces.

Numerical simulation. To simulate our system in one dimension, we integrated the discretized equations of the chain-of-springs model (see for example Supplementary equation (5)) using a simple Euler method. We used a time step of numerical integration $\delta t = 0.25$ min, which is an order of magnitude smaller than any other timescale in the problem. The length scale was set by the average homeostatic cell length $\langle l \rangle = 1$, with spatial derivatives taken as difference to the nearest neighbour. We simulated a chain of N cells, with labels i , ERK activity E_i , preferred length l_0^* , length $l_i = r_{i+1} - r_i$ and polarity p_i .

To simulate confluent tissues, we used periodic boundary conditions. To simulate monolayer expansion, we first simulated the system for 100 min without leader cells or boundary expansion before release (to allow for ERK dynamics to equilibrate), and complemented the problem with a boundary condition at the free edge such that cell polarity approached $p_N = p_b$. This provided a fixed polarity to leader cells at the edge of the monolayer (as observed experimentally, see ref.⁸). We also applied small amounts of white noise of amplitude $\eta_E = 0.05$ to the equation of ERK dynamics.

To simulate optogenetically applied ERK waves of frequency ω and wavevector q and construct Fig. 3d, we imposed travelling waves $E(x, t) = E_0 \cos(\omega t + qx)$ over a domain with periodic boundary conditions and monitored the average response of other variables (in particular cellular displacement as a proxy for polarization) after 10 temporal periods of oscillation. In order to find a simple analytical solution for average polarity in the presence of an applied ERK wave, and construct Fig. 3e and Extended Data Fig. 8a, we made several assumptions: we neglected traction forces and diffusion of polarity, as well as advection of ERK, rest length and polarity. In contrast, we included all of these effects in numerical simulations of applied waves and of the fully coupled system (Fig. 3d, Extended Data Fig. 8d, Fig. 4 and Extended Data Fig. 9), with the comparable analytical and numerical results (Extended Data Fig. 8) showing little qualitative difference. Since the inclusion of these effects made little difference we then returned when studying alternative couplings for symmetry breaking (Supplementary Section

II F) to working with continuous models without extra diffusion or advection terms and numerically solved the system of equations for an applied wave using Mathematica's NDSolve to produce Extended Data Fig. 7.

To simulate the experiments of uniform activation (resp. inhibition of ERK) shown in Extended Data Fig. 2c, or the nonlinear analysis of patterns for values of α/β above the critical point shown in Extended Data Fig. 3, we used the same simulation as above for confluent tissues, with the only change being to add a constant term to the equation of ERK, which then read

$$\tau_E \partial_t E = E_0 - E - E^3 + \beta \partial_x r. \quad (10)$$

Given that ERK levels in the control simulation oscillate between the range of -0.15 and $+0.15$, we set $E_0 = 0.25$ (resp. $E_0 = -0.25$) to simulate global ERK activation (resp. inhibition) and plotted the corresponding dynamics for local ERK activity and cell length (Extended Data Fig. 2c). This demonstrated a marked inhibition of density waves in both conditions, in agreement with experimental data (Extended Data Fig. 1).

Parameter estimation. A major assumption of our model is the bidirectional coupling between ERK activity and cellular length, characterized by timescales τ_E and τ_l and coupling strengths α and β . Ideal experiments for constraining these parameters are described in ref. ²⁷: they consist of (1) applying abrupt mechanical strains while observing ERK response (mechanical stretching experiments combined with FRET sensors, Fig. 2a), and conversely (2) applying abrupt changes in ERK activity while observing mechanical response (optogenetic ERK activation experiments, Fig. 2c). Below, we detail our theoretical interpretation and statistical analysis of each of these experiments.

Mechanical stretching experiments. The cellular stretching experiment is relatively straightforward to fit since it involves only the equation on ERK (equation (3)). At time $t = 0$ an abrupt, uniform and permanent strain $\Delta\epsilon = 50\%$ is applied to the cellular monolayer. We model this as a Heaviside stretch $\Delta\epsilon H(t)$:

$$\tau_E \partial_t E = -E + \beta \Delta\epsilon H(t), \quad (11)$$

which predicts that ERK follows

$$E(t) = \beta \Delta\epsilon (1 - e^{-t/\tau_E}), \quad (12)$$

and allows us to estimate τ_E and β (Fig. 2b and Extended Data Fig. 5a). We examined average ERK activity in three independent repetitions of the stretch experiment (at least $n = 685$ averaged cells in each), and found good agreement for $\tau_E = 6 \pm 2$ min, $\beta = 0.56 \pm 0.06$ and $E_{eq} = 0.66 \pm 0.05$ (mean \pm standard deviation) at a single optimum. Fitting was performed using a standard gradient descent routine (Broyden–Fletcher–Goldfarb–Shanno, BFGS) from SciPy optimized with a least-squares error function. We note that the applied stretch is larger than the stretch typically experienced by wild-type cells, potentially causing a saturation of ERK activation and underestimation of β .

Optogenetic experiments. The optogenetic ERK activation experiment involves both the equations on cell displacement and rest length (equations (1) and (2)). When ERK is activated in a half-plane, the system is symmetric parallel to the boundary, so we modelled in one dimension with a Heaviside function for the optogenetic ERK activation:

$$\tau_r \partial_t r = \partial_{xx} r - \partial_x l_0 \quad (13a)$$

$$\tau_l \partial_t l_0 = -l_0 - \alpha(\Delta E H(x) + E_0), \quad (13b)$$

which after non-dimensionalization using $T = \tau_l$ and $L = a\sqrt{\tau_l/\tau_r}$, with a the average cell size that we set to unity, reads

$$\partial_t r = \partial_{xx} r - \sqrt{\frac{\tau_l}{\tau_r}} \partial_x l_0 \quad (14a)$$

$$\partial_t l_0 = -l_0 - \alpha \sqrt{\frac{\tau_r}{\tau_l}} (\Delta E H(x) + E_0). \quad (14b)$$

The second equation is solved independently to give $l_0(x, t) = \alpha \sqrt{\frac{\tau_r}{\tau_l}} (e^{-t} - 1)(\Delta E H(x) + E_0)$ that we substitute into the equation on displacement to give

$$\partial_t r = \partial_{xx} r + \alpha \Delta E (1 - e^{-t}) \delta(x) \quad (15)$$

This describes diffusion from an exponential point source, but can be reformulated as diffusion from a constant point source on new variable $\mathbf{m}(x, t) = \mathbf{r}(x, t) + \partial_t \mathbf{r}(x, t)$:

$$\partial_t m = \partial_t(r + \partial_t r) = \partial_{xx} m + \alpha \Delta E \delta(x) \quad (16)$$

This is solved by integrating the solution for an instantaneous point source to give

$$m(x, t) = \int_0^t \frac{\alpha \Delta E}{4\pi t} \exp\left[\frac{-x^2}{4t}\right] dt = \alpha \Delta E \left(\sqrt{\frac{t}{\pi}} \exp\left[\frac{-x^2}{4t}\right] + \frac{x}{2} \operatorname{erf}\left[\frac{x}{2\sqrt{t}}\right] - \frac{|x|}{2} \right) \quad (17)$$

Finally, solving for $\mathbf{r}(x, t)$ using the definition of $\mathbf{m}(x, t)$ provides results for the displacement

$$r(x, t) = \frac{\alpha \Delta E}{2} \left(|x| \left(\operatorname{erf}\left[\frac{|x|}{2\sqrt{t}}\right] - 1 \right) + e^{-t} \left(-ie^{-i|x|} + 2\sqrt{\frac{t}{\pi}} \exp\left[t - \frac{x^2}{4t}\right] - e^{ix} \operatorname{erfi}\left[\sqrt{t} - \frac{ix}{2\sqrt{t}}\right] \right) \right) \quad (18)$$

and velocity

$$\partial_t r(x, t) = \frac{\alpha \Delta E}{2} e^{-t} \left(ie^{i|x|} + e^{ix} \operatorname{erfi}\left[\sqrt{t} - \frac{ix}{2\sqrt{t}}\right] \right) \quad (19)$$

Note that $r(x, t)$ describes the field of cellular deformations—interpreted as the displacement after time t of a cell that starts a distance x from the boundary—that we tracked in order to fit parameters. Because the initial displacement is controlled by contraction of only the first cell layer, we could estimate $\tau_l = 100–140$ min using only the solution of the boundary (Fig. 2d,e) and the power law on $\mathbf{m}(0, t)$

$$m(0, t) = \frac{\alpha \Delta E}{\sqrt{\pi}} t^{1/2} \quad (20)$$

$$r(0, t) = \frac{\alpha \Delta E}{\sqrt{\pi}} t^{1/2} - \frac{\alpha \Delta E}{2} e^{-t} \operatorname{erfi}\left(t^{1/2}\right) \quad (21)$$

$$\partial_t r(0, t) \equiv v(0, t) = \frac{\alpha \Delta E}{2} e^{-t} \operatorname{erfi}\left(t^{1/2}\right) \quad (22)$$

When dimensions are added back $\mathbf{m}(0, t)$ becomes

$$Lm = r + \tau_l v = L \frac{\alpha \Delta E}{\sqrt{\pi}} \left(\frac{t}{\tau_l}\right)^{1/2} = \frac{\alpha \Delta E}{\sqrt{\pi}} \left(\frac{t}{\tau_r}\right)^{1/2}, \quad (23)$$

or in log-log space

$$\log(Lm) = \log(r + \tau_l v) = \log\left(\frac{\alpha \Delta E}{\sqrt{\pi \tau_r}}\right) + \frac{1}{2} \log(t). \quad (24)$$

Since τ_r controls how quickly deformation spreads into the bulk we estimate it instead using the full solution for displacement (equation (18)) to give $\tau_r = 5–16$ min (Fig. 2f and Extended Data Fig. 5b–d). We can also resolve α from estimates of $\alpha \Delta E$ (Extended Data Fig. 5b–d) using the observation that the step in optogenetic ERK activity is typically around one tenth of the initial value ($\Delta E/E_0 \approx 0.1$) to give $\alpha = 8 \pm 2$ (mean \pm standard deviation). We note however that, as for estimates of β , α is likely underestimated, because we neglect the natural ERK response of the non-activated patch of cells in response to stretching by the activated ERK patch, which would tend to decrease the overall amplitude of contraction. This would explain why the coefficients of coupling that we infer are smaller than the predicted threshold of the instability (Supplementary Section I B).

Data analysis and fitting. The optogenetic experiments (Fig. 2c) used raw data from ref. ²⁷ and consisted of $N = 3$ independent repeats, with each repeat consisting of $n = 3$ fields of view along the expanding monolayer. To quantify the boundary displacement we averaged the displacement from initial position $\mathbf{r}(0, t)$ across all three fields of view for each repeat and calculated velocity $v(0, t)$ using a standard NumPy routine for central differences. To measure bulk displacement we tracked cell centres $\mathbf{r}(x, t)$ using Imaris software and binned cells from each repeat according to initial distance from the boundary x . To account for the heterogeneity in cell responses, we fitted each repeat independently to report the broad range of parameter values (Fig. 2d,e and Extended Data Fig. 5b–d), and also averaged all three to perform the collective bulk fitting in Fig. 2f. For fitting we used standard gradient descent (BFGS from SciPy), with a least-squares error function and discovered unique minima in all cases (see Extended Data Fig. 6 for identifiability). We set the zero point ($t = 0$) to 10 min (that is, two timepoints) after illumination to account for the transient in ERK activation in response to the optogenetic switch, which occurs on timescales of τ_E (that is, to account for the lack of an instantaneous activation as assumed in the model) and discarded the next two timepoints to avoid any remaining bias from this transient. We first fit the boundary (equation (24)) to estimate τ_l before fixing τ_l using these values to estimate τ_r from the bulk (equation (18)). For the collective fit in Fig. 2f we fixed τ_l using the average value from the repeats of fits of the boundary.

Overview of parameters and variables.

Here, we provide an overview of the variables used in the study:

- $\mathbf{r}(x, t)$: displacement at position x and time t
- $E(x, t)$: local ERK activity in a cell at position x and time t
- $l_0(x, t)$: cellular rest length (that is, the length the cell would adopt in the absence of external stresses or constraints) at position x and time t
- $l(x, t)$: cellular length at position x and time t
- $p(x, t)$: cellular polarity at position x and time t , driving polar active migration

Here, we provide an overview of the parameters used in the study:

- $\tau_r = \zeta/k$: timescale of mechanical diffusion over one cell length, which quantifies how quickly stress propagates in the monolayer under frictional contact with the substrate. Also viewed as the ratio of the coefficient of friction with substrate ζ to cell stiffness k . Fitted to $\tau_r \approx 10$ min from our optogenetic experiments (Fig. 2).
- τ_E : timescale of ERK relaxation/dynamics, assuming first-order kinetics. Fitted to $\tau_E \approx 6$ min from our cell stretching experiments (Fig. 2).
- τ_f : timescale of cell resting area dynamics, assuming first-order kinetics. Fitted to $\tau_f \approx 120$ min from our cell optogenetic experiments (Fig. 2).
- α and β : strength of the mechanochemical couplings, resp. from ERK activity on cell rest length and from cell length on ERK activity. Only their product $\alpha\beta$ is relevant for the onset of instability, so we performed simulations in Fig. 4 for $\alpha\beta = 1.2\alpha\beta_{crit}$. Sensitivity analysis for the influence of different ratios α/β is shown in Extended Data Fig. 2.
- τ_p : timescale of polarity dynamics. Constrained to 15–40 min from literature^{15,40,41}, although the effect of parameter values outside this range was explored computationally (Fig. 3). Figure 4 uses $\tau_p = 30$ min as a typical value within this range.
- γ : strength of the coupling from gradients of stress on cellular polarity. Either taken as a constant, or nonlinearly dependent on ERK. Value not constrained by data, although absolute value simply rescales traction force. We use $\gamma = 0.5$ in Fig. 4a,b (wild-type) and $\gamma = 0.05$ in Fig. 4c to simulate impaired directionality sensing corresponding to the Merlin knockout condition.

Reporting Summary. Further information on research design is available in the Nature Research Reporting Summary linked to this article.

Data availability

The data that support the plots within this paper and other findings of this study are available from the corresponding authors upon reasonable request. Raw movies

for Figs. 1–4 are available at <https://doi.org/10.24631/ssbd.repos.2020.07.002>. Source data are provided with this paper.

Code availability

All code used in this study is available from the corresponding authors upon reasonable request.

References

54. Naito, Y., Hino, K., Bono, H. & Ui-Tei, K. CRISPRdirect: software for designing CRISPR/Cas guide RNA with reduced off-target sites. *Bioinformatics* **31**, 1120–1123 (2015).

Acknowledgements

We would like to thank G. Tkacik and all of the members of the Hannezo and Hirashima groups for useful discussions, X. Trepat for help on traction force microscopy and M. Matsuda for use of the lab facility. E.H. acknowledges grants from the Austrian Science Fund (FWF) (P 31639) and the European Research Council (851288). T.H. acknowledges a grant from JST, PRESTO (JPMJPR1949). This project has received funding from the European Union's Horizon 2020 research and innovation programme under the Marie Skłodowska-Curie grant agreement no. 665385 (to D.B.), from JSPS KAKENHI grant no. 17J02107 (to N.H.) and from the SPIRITS 2018 of Kyoto University (to E.H. and T.H.).

Author contributions

Supervision and project conceptualization: T.H. and E.H. Theory and simulations: D.B., N.R. and E.H. Data analysis: D.B., N.H., N.R., T.H. and E.H. Experiments: N.H. and T.H. Manuscript writing: D.B., T.H. and E.H., with input from all authors.

Competing interests

The authors declare no competing interests.

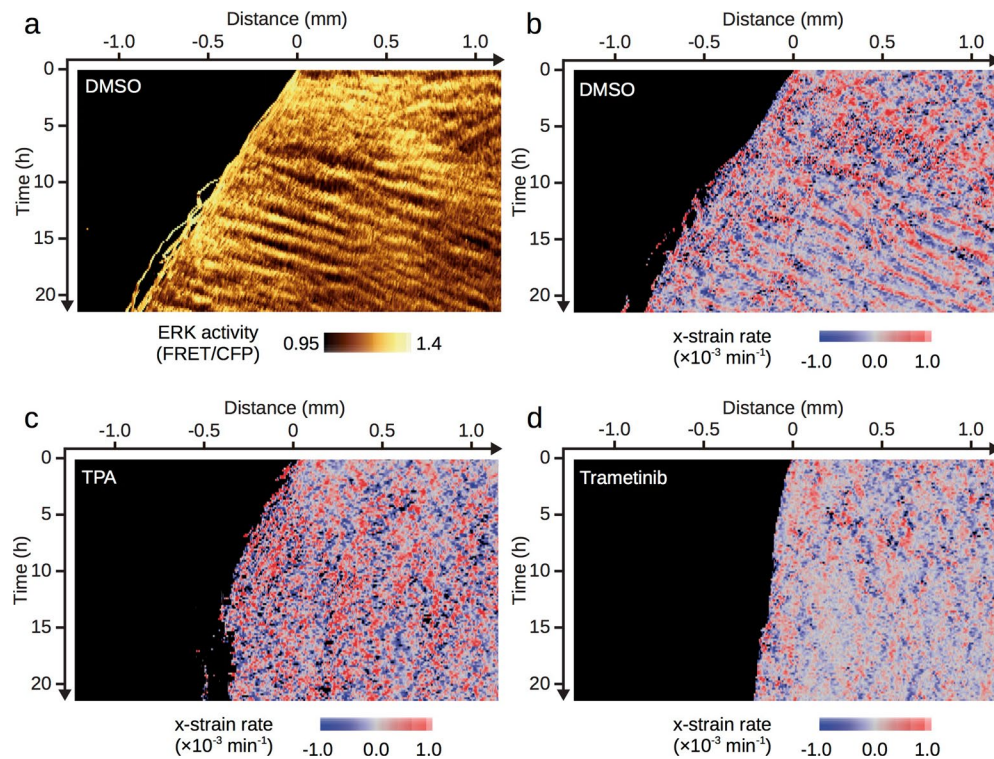
Additional information

Extended data is available for this paper at <https://doi.org/10.1038/s41567-020-01037-7>.

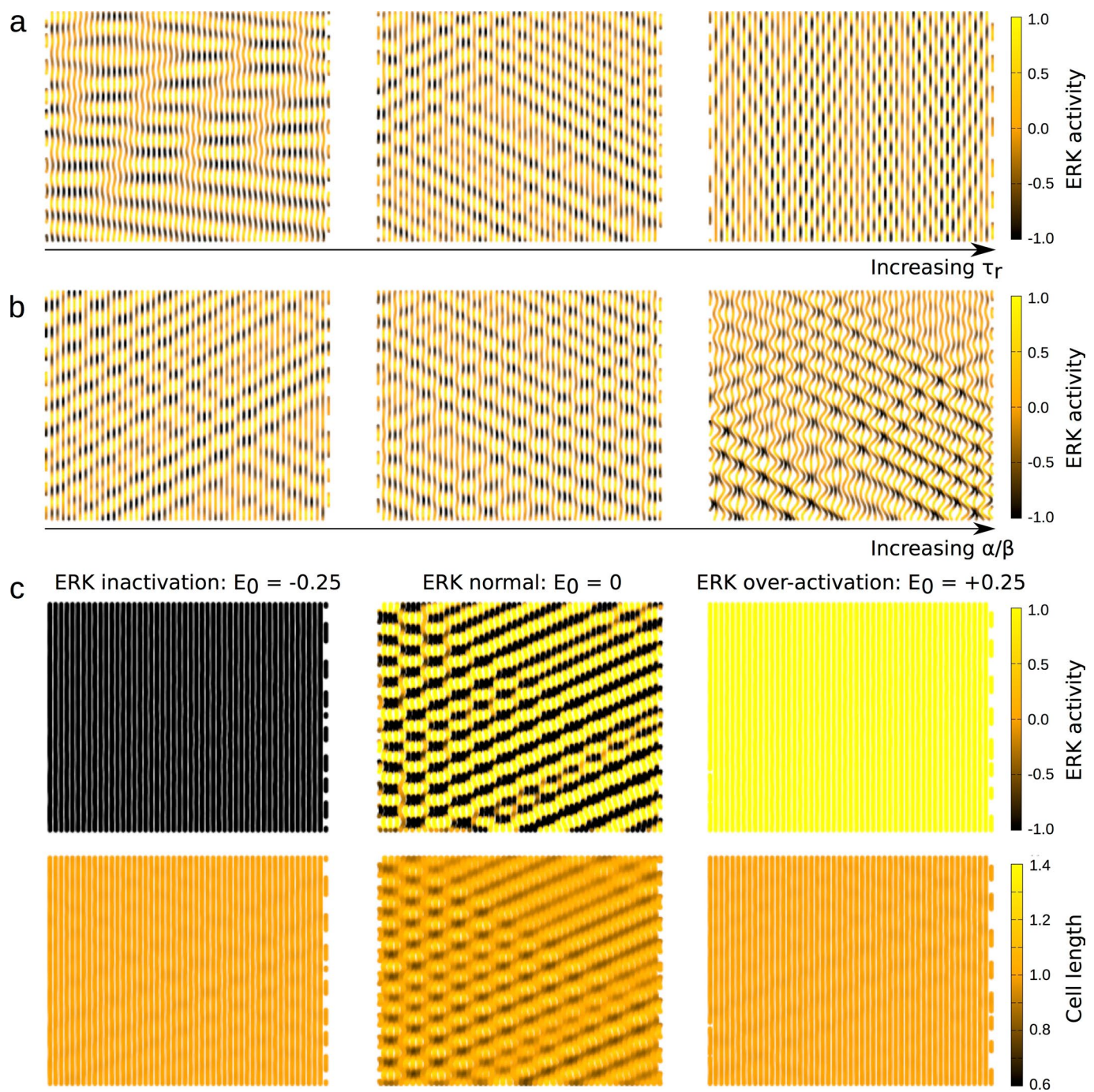
Supplementary information is available for this paper at <https://doi.org/10.1038/s41567-020-01037-7>.

Correspondence and requests for materials should be addressed to T.H. or E.H.

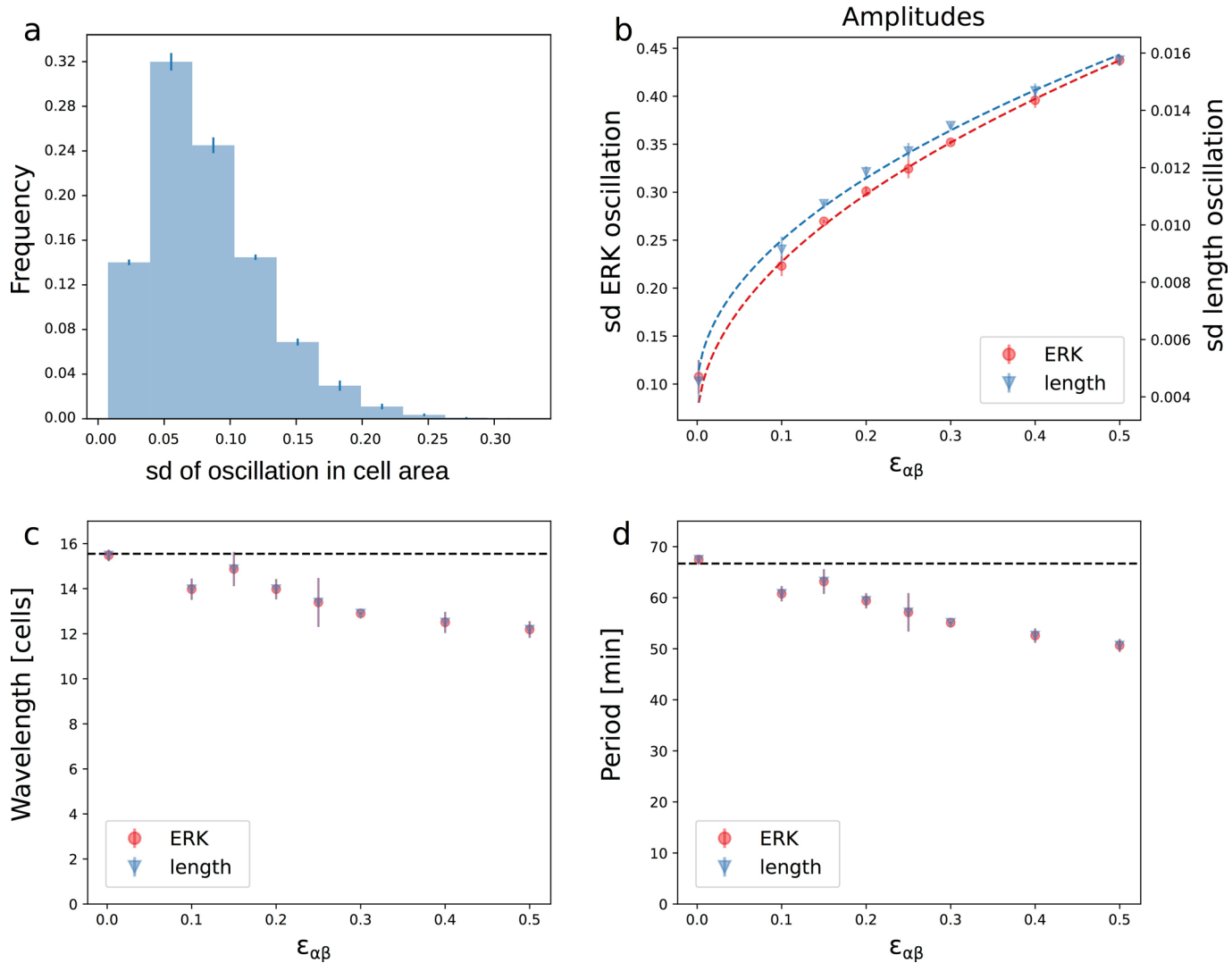
Reprints and permissions information is available at www.nature.com/reprints.



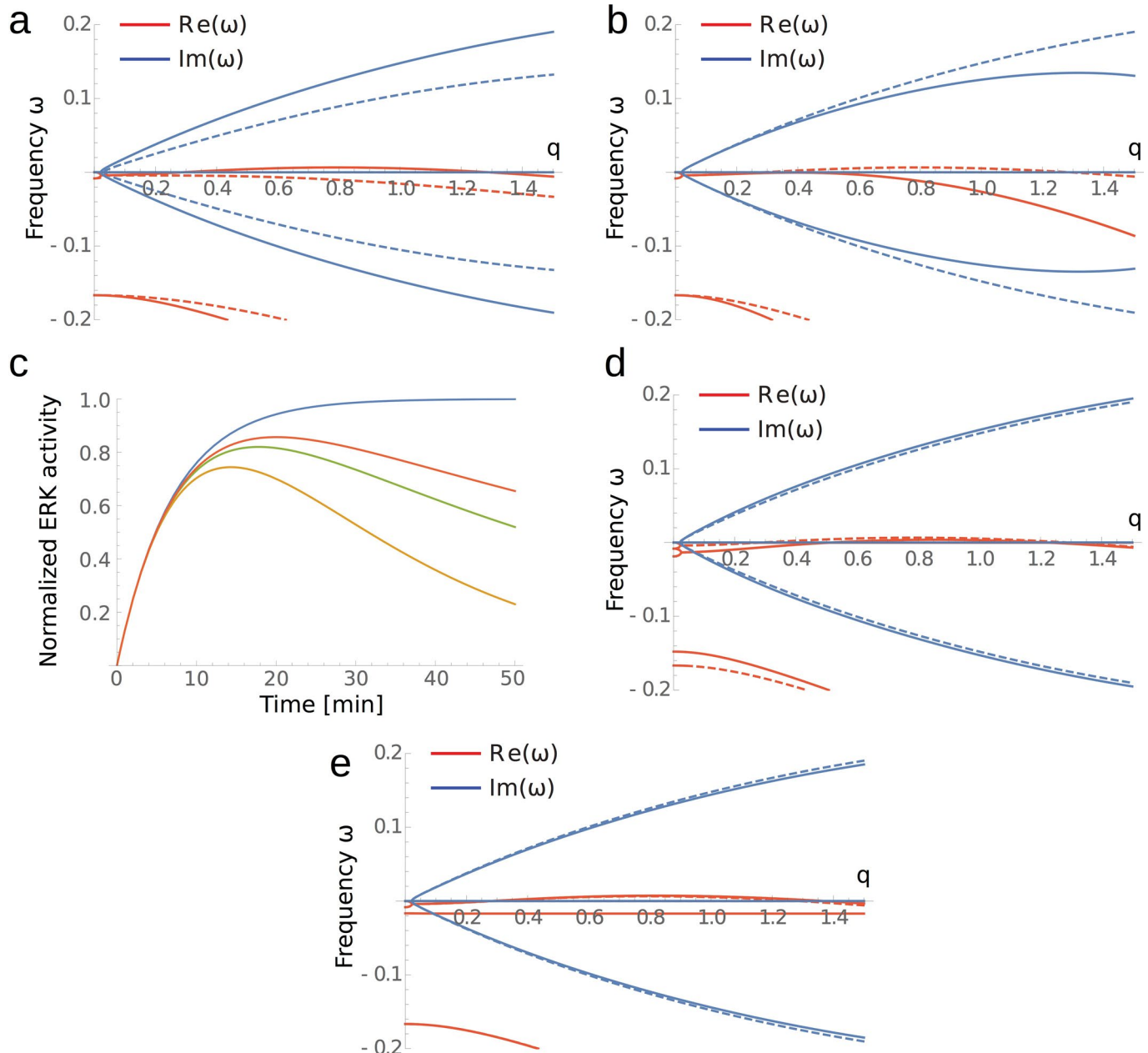
Extended Data Fig. 1 | Over-activation or inhibition of ERK causes loss of density waves. **a,b**, DMSO controls showing WT behaviour of ERK (a) and density waves (b, visualized by x-strain rate analysis, see Methods for details). **c,d**, Drug treatments to overactivate ERK (TPA at 10 nM) or inactivate ERK (Trametinib at 200 nM) cause loss of density waves (as well as changes in traction forces, as shown in ref. ⁹), suggesting that ERK is a core part of the mechano-chemical instability and not just a downstream component.



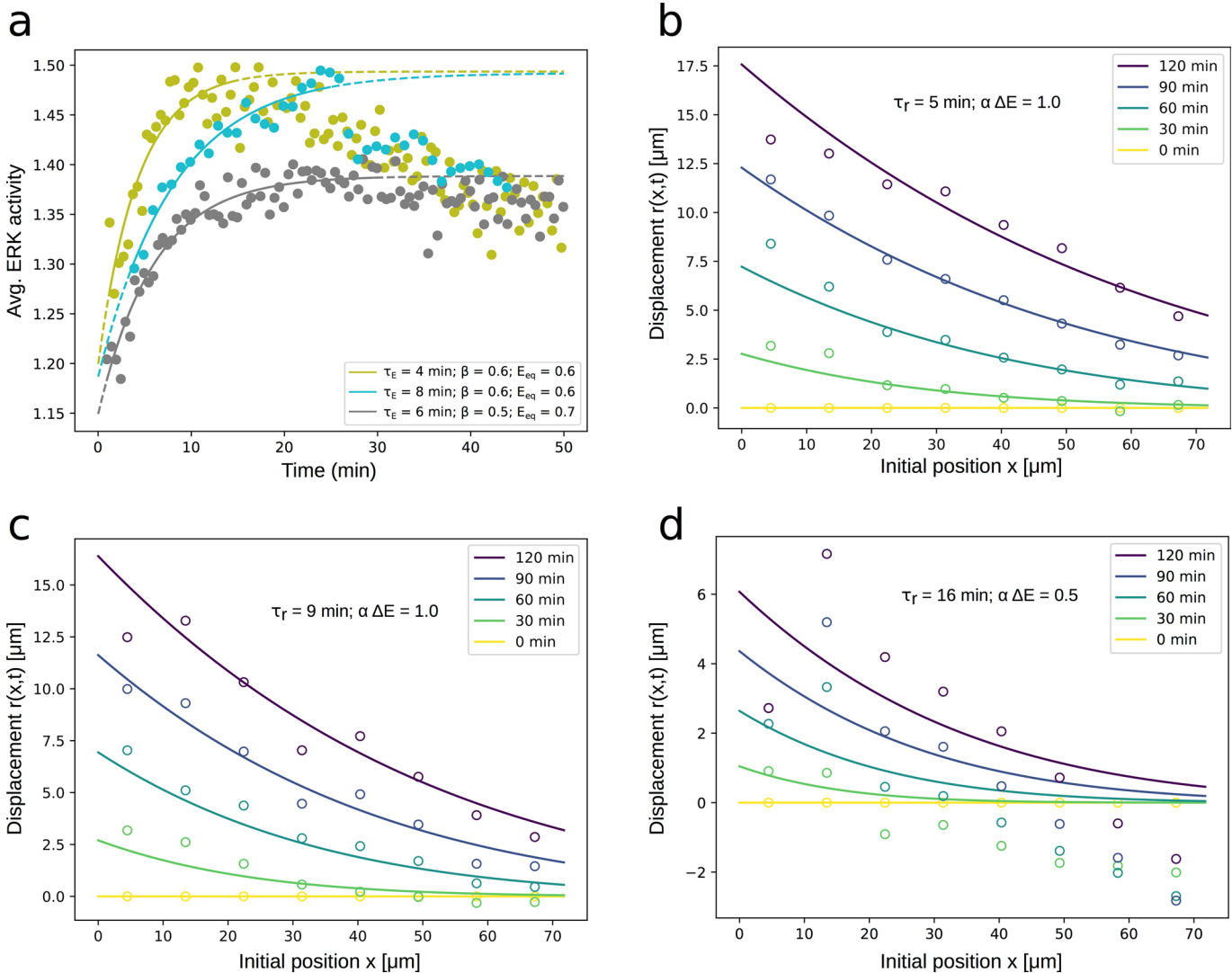
Extended Data Fig. 2 | Effect of varying parameters on simulated dynamics of confluent tissue. **a**, Increasing the timescale of mechanical relaxation $\tau_r = \zeta/k$ (i.e. the ratio of substrate friction to cell stiffness) shortens the wavelength of the instability without changing the period. Colours represent ERK activity. **b**, Increasing the ratio of mechano-chemical coupling constants α/β results in larger cell deformation without affecting the wavelength or period of the instability. All simulations use $\alpha\beta = 1.2 \times \alpha\beta_{crit}$. **c**, Waves of both ERK and density are suppressed by either inhibition or over-activation of ERK (See Eq. 10 in Methods).



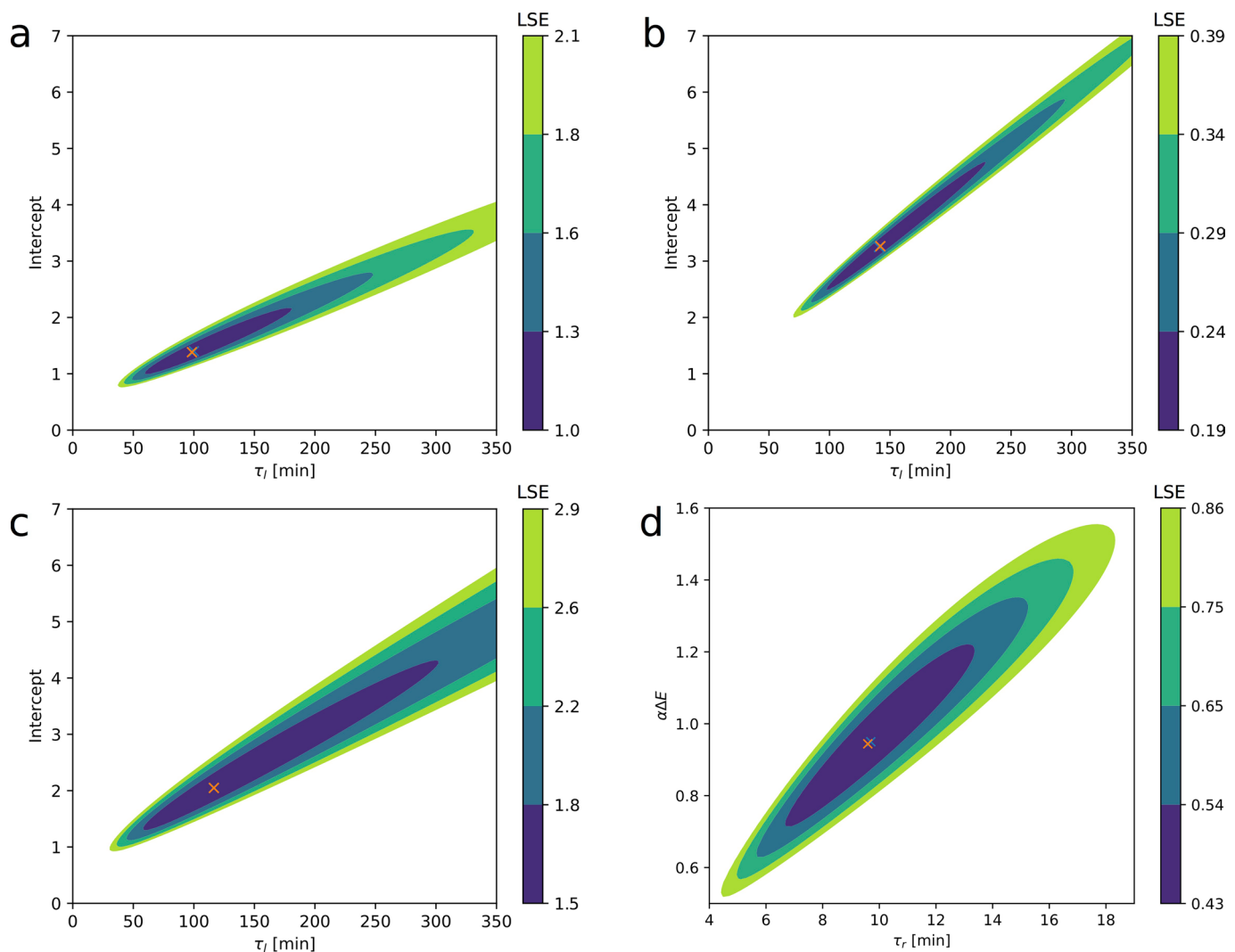
Extended Data Fig. 3 | Amplitude of oscillations and nonlinear behaviour of the model. **a**, Distribution of oscillation amplitude in cell area in confluent tissue (quantified by the normalized standard deviations of area for time traces of individual tracked cells, $n=3$ experiments, with error bars showing standard deviation of frequencies between experiments, see Methods for details). Standard deviations were normalized by mean area for each cell to give a fractional deviation from the mean. Typical oscillations of 5 to 10 % are small enough to justify the use of a linear mechanical model. **b**, In 1D simulations, steady state amplitudes of ERK and cell length l , which are stabilised by non-linear terms, follow an expected power law dependence on the distance from the critical point $\sim \epsilon_{\alpha\beta}^{1/2} = (\alpha\beta/\alpha\beta_{crit} - 1)^{1/2}$. **c,d**, The wavelength and period of the instability decrease gradually with distance from the critical point, although they both remain close to the predictions from linear stability (black dashed line) even at distances of around $1.5 \times \alpha\beta_{crit}$.



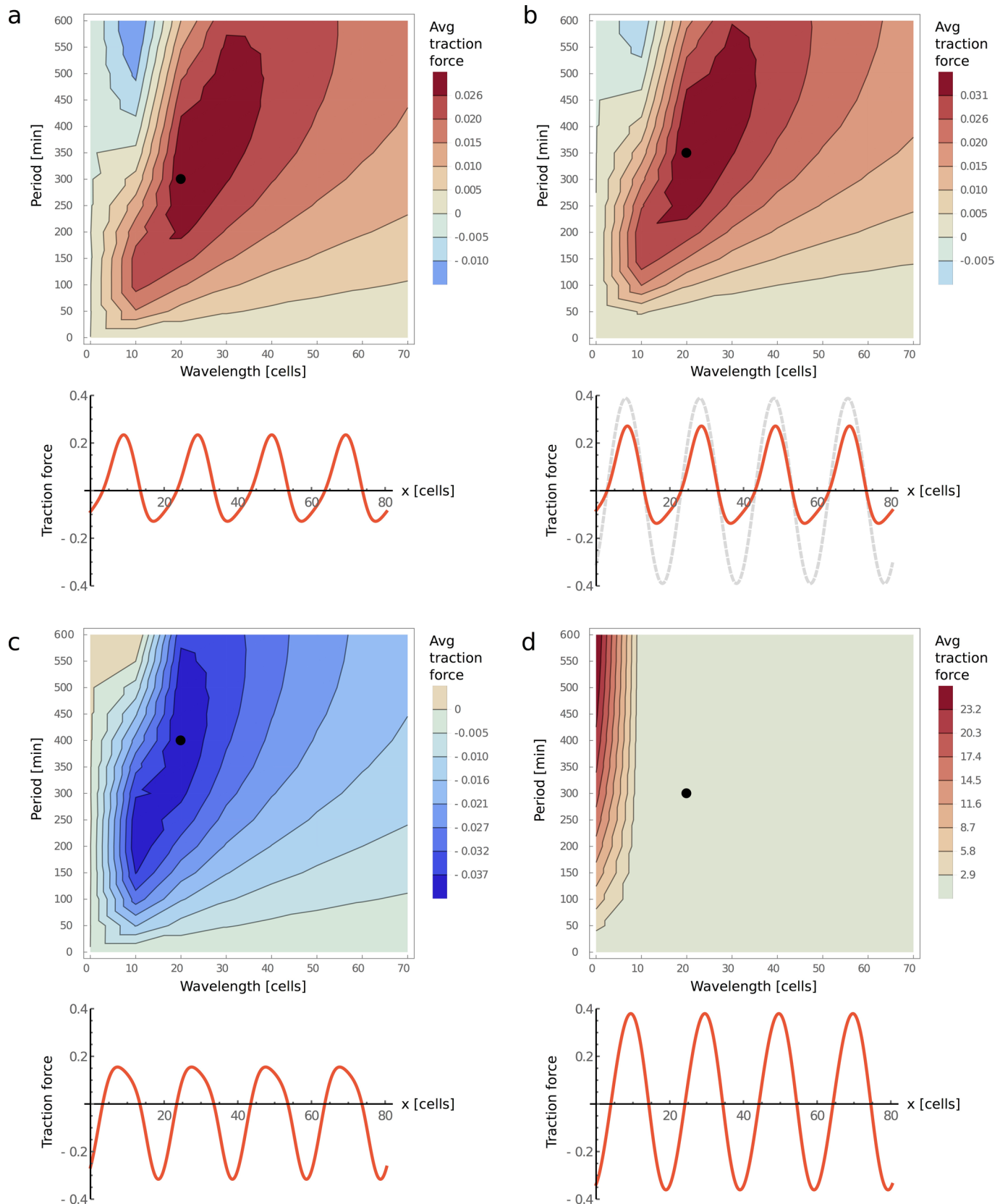
Extended Data Fig. 4 | Effect of different couplings on pattern formation. **a**, Angular frequency ω as a function of wavevector q for the model presented in the main text (Eq. 4) for values of $\alpha\beta$ at $1.4 \times \alpha\beta_{crit}$ (solid) and $0.6 \times \alpha\beta_{crit}$ (dashed), i.e. above and below the threshold for the instability. Positive values of the real part of ω (red) indicate instability whereas finite values of the imaginary part of ω (blue) indicate oscillations. **b**, Little changes qualitatively to this picture when we include diffusion of ERK at a realistic rate $D = 1 \text{ cell}^2/\text{min}$ (solid lines; dashed lines $D \rightarrow 0$). **c**, We can also account for the ERK desensitization (Eq. S24) seen in cell stretch (Fig. 2b) and optogenetic perturbation experiments (see [11]) (plotted $\tau_d = 30 \text{ min}$ (yellow), 60 min (green) 90 min (red) and $\tau_d \rightarrow \infty$ (blue)). **d**, But for realistic timescales this has little effect on parameter estimates or on the dispersion relation governing emergent patterns (solid lines $\tau_d = 60 \text{ min}$, dashed lines $\tau_d \rightarrow \infty$). **e**, Similarly, incorporating Maxwellian visco-elasticity in the model (see section Section II E in the SI Text) has little effect on the dispersion relation for realistic viscoelastic timescales ($\tau_m = 60 \text{ min}$).



Extended Data Fig. 5 | Individual fits of repeats from cell stretch and optogenetic activation experiments. **a**, Individual fits of the three independent repeats of cell stretch collectively fit in Fig. 2b. **b-d**, Individual fits of the three independent repeats for bulk displacement after ERK activation that were averaged and collectively fit in Fig. 2f. In d) displacements are distorted due to the coincidence of a natural contraction wave pre-existing the optogenetic activation of ERK which makes the data difficult to fit. We therefore left τ_r free but fixed $\alpha \Delta E = 0.5$ using a steady-state assumption on Eq. 13 (see Methods) and observation of roughly 50% difference in final cell size either side of the optogenetic boundary.

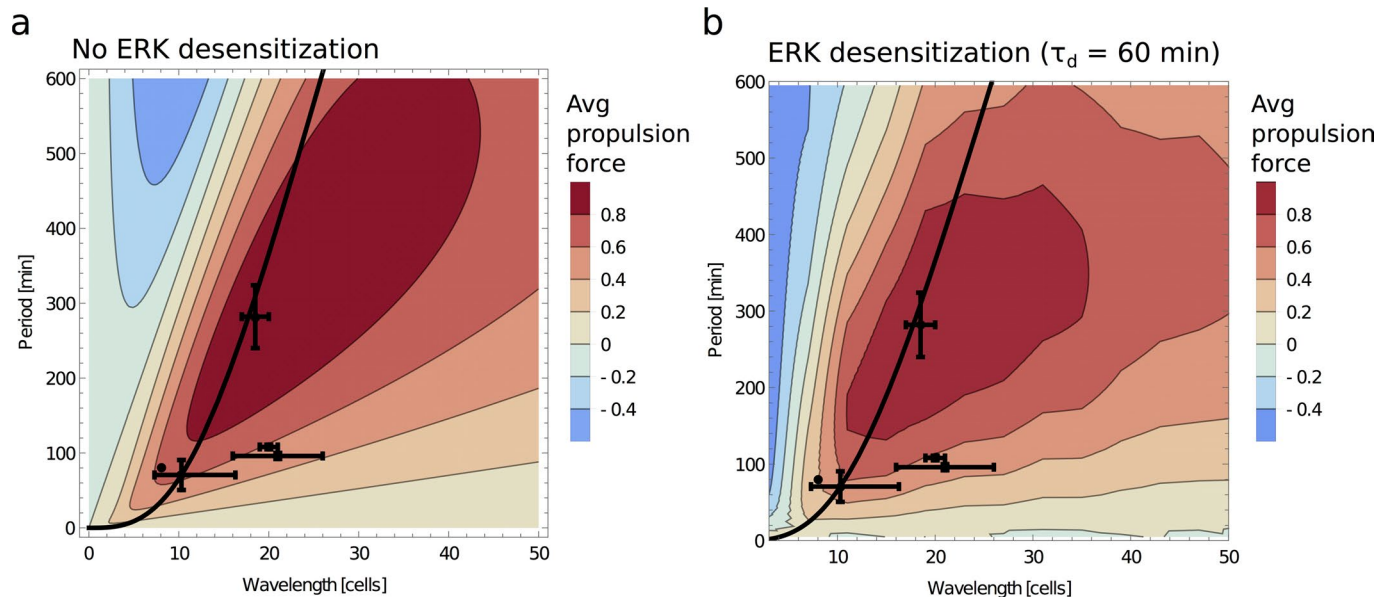


Extended Data Fig. 6 | Identifiability of τ_i and τ_r . **a-c**, Least squares error in the fits of boundary displacement (see Methods for details) from the optogenetic ERK activation (each plot shows a fit to each of the $n=3$ individual experiments). **d**, Least squares error in the fit of bulk displacement averaged over the same independent repeats. τ_i was fixed to the values found in panels (a-c), and the free parameters τ_r and $\alpha\Delta E$ were fitted. Simple gradient descent finds unique values for both τ_i (a-c) and τ_r (d).

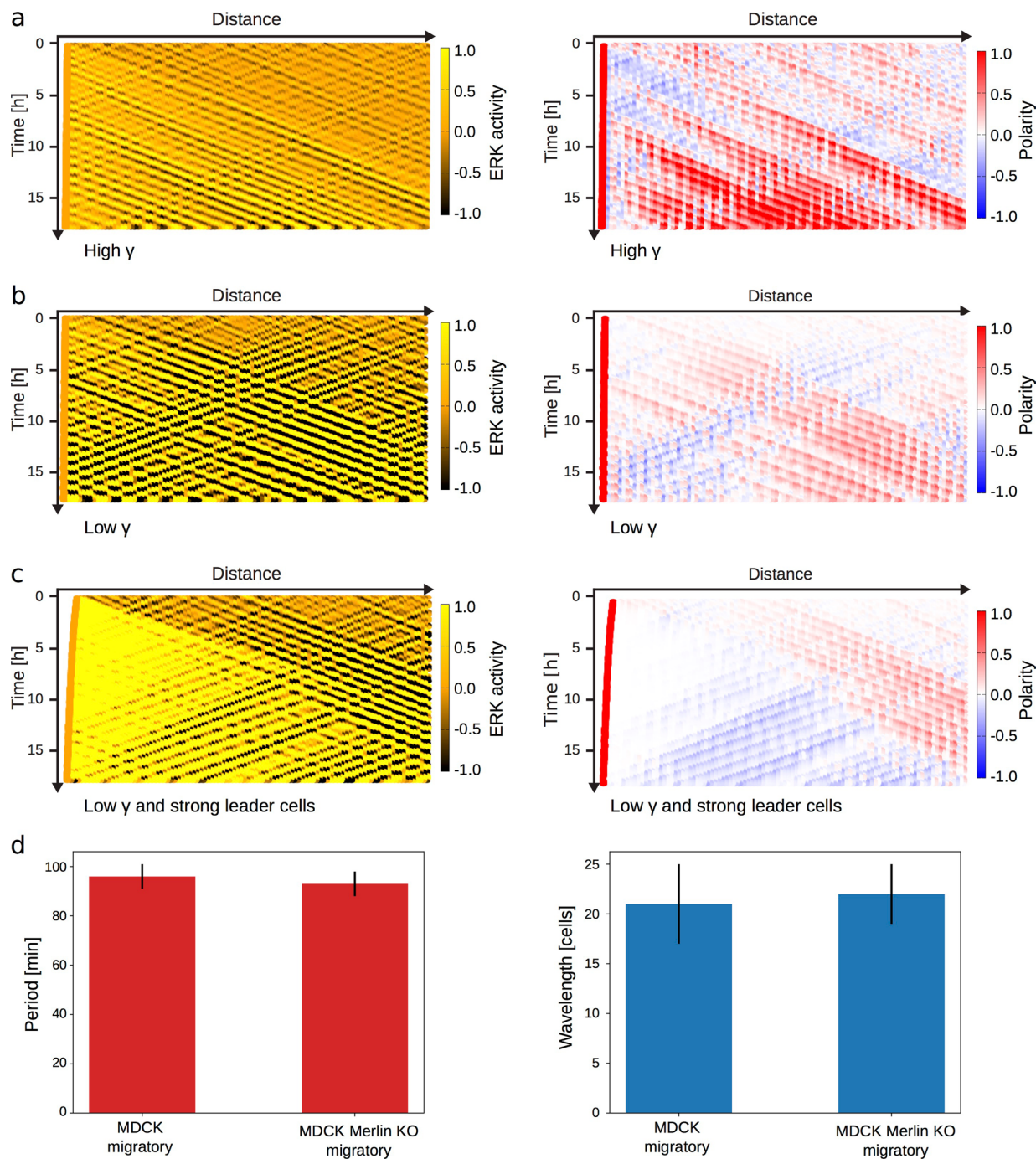


Extended Data Fig. 7 | See next page for caption.

Extended Data Fig. 7 | Net traction force in response to applied ERK waves for different model non-linearities. Positive average traction forces represent net migration opposite to the direction of propagation of ERK waves. Spatial profiles of traction force (red curves) and polarity (grey curves) correspond to the points indicated in the contour plots. **a**, Sigmoidal $\gamma(ERK)$ (coupling between polarity and gradients of stresses as a decreasing function of ERK) as in main text **b**) Sigmoidal traction force coefficient (decreasing function of ERK) **c**) Sigmoidal stiffness $k(ERK)$ (increasing function of ERK) with active reference length **d**) Sigmoidal stiffness $k(ERK)$ (increasing function of ERK) with active stress. All simulation were performed on equivalent dimensionless models with parameters $\tau_i = 120$ min, $\tau_r = 10$ min, $\tau_p = 15$ min and $\gamma_0 = 0.1$. We used a sigmoidal non-linearity of the form $f(ERK) = 1/(1 + \exp[\pm ERK])$ with \pm for either decreasing or increasing dependencies. For cases a) c) and d), profiles of polarity and traction forces are identical after a rescaling. In contrast, for case b), traction forces can be different from polarity due to the non-linearity. Then, average traction forces may be non-zero (red curve) but net polarity remains close to zero everywhere (grey curve), which is contrary to experimental findings (Fig. 3a). We use a lower estimate of $\tau_p = 15$ min to show that cases a) and b) are distinguishable by their polarity profiles even in the limit $\tau_p \rightarrow 0$ where traction forces converge. See SI Text Section II F for further details on the different models.



Extended Data Fig. 8 | Effect of ERK desensitization on optimal polarity. **a-b**, ERK desensitization (Eq. S24) at realistic timescales ($\tau_d = 60$ min) decreases average polarization/traction forces at long wavelengths and periods. The absolute optimum is little affected, moving from $\lambda = 22$ cells $T = 312$ min to $\lambda = 19$ cells $T = 285$ min. See SI Text Section I C for details on data points. (Note that b is a repeat of Fig. 3d in the main text.).



Extended Data Fig. 9 | Unidirectional waves and long-range polar order require stress-polarity coupling and active migration. **a**, In wild-type simulations (Eq. S14), emergent ERK/density waves orient away from the edge (left) and induce a counter polarization/active migration in the bulk (right). **b**, When stress-polarity coupling is weak (small γ , mirroring Merlin KO), ERK waves still emerge (left) but do not induce strong enough polarization/active migration to allow for unidirectional orientation and long-range polar order (right). **c**, Alternatively, when weak stress-polarity coupling is accompanied by strong leader cells (3 times stronger polarity at leading edge), ERK waves propagate towards the migrating front (left) and bulk polarity is established in the opposite direction (right). Note that a and b correspond to Fig. 4a and c of the main text. **d**, Waves with the same wavelength ($p=0.7791$, two-sample t-test) and period ($p=0.7780$, two-sample t-test) emerge in Merlin KOs and wild-type suggesting that active migration is not driving the instability. Error bars indicate standard deviation.

Reporting Summary

Nature Research wishes to improve the reproducibility of the work that we publish. This form provides structure for consistency and transparency in reporting. For further information on Nature Research policies, see our [Editorial Policies](#) and the [Editorial Policy Checklist](#).

Statistics

For all statistical analyses, confirm that the following items are present in the figure legend, table legend, main text, or Methods section.

n/a Confirmed

- The exact sample size (n) for each experimental group/condition, given as a discrete number and unit of measurement
- A statement on whether measurements were taken from distinct samples or whether the same sample was measured repeatedly
- The statistical test(s) used AND whether they are one- or two-sided
Only common tests should be described solely by name; describe more complex techniques in the Methods section.
- A description of all covariates tested
- A description of any assumptions or corrections, such as tests of normality and adjustment for multiple comparisons
- A full description of the statistical parameters including central tendency (e.g. means) or other basic estimates (e.g. regression coefficient) AND variation (e.g. standard deviation) or associated estimates of uncertainty (e.g. confidence intervals)
- For null hypothesis testing, the test statistic (e.g. F , t , r) with confidence intervals, effect sizes, degrees of freedom and P value noted
Give P values as exact values whenever suitable.
- For Bayesian analysis, information on the choice of priors and Markov chain Monte Carlo settings
- For hierarchical and complex designs, identification of the appropriate level for tests and full reporting of outcomes
- Estimates of effect sizes (e.g. Cohen's d , Pearson's r), indicating how they were calculated

Our web collection on [statistics for biologists](#) contains articles on many of the points above.

Software and code

Policy information about [availability of computer code](#)

Data collection Metamorph (Molecular Devices, Sunnyvale, CA) was used for time-lapsing microscopy.

Data analysis All the data in this study were analyzed by Metamorph (Molecular Devices, Sunnyvale, CA), Fiji TrackMate plugin, and MATLAB (Mathworks, Natick, MA). The codes are available from the corresponding authors on reasonable request.

For manuscripts utilizing custom algorithms or software that are central to the research but not yet described in published literature, software must be made available to editors and reviewers. We strongly encourage code deposition in a community repository (e.g. GitHub). See the Nature Research [guidelines for submitting code & software](#) for further information.

Data

Policy information about [availability of data](#)

All manuscripts must include a [data availability statement](#). This statement should provide the following information, where applicable:

- Accession codes, unique identifiers, or web links for publicly available datasets
- A list of figures that have associated raw data
- A description of any restrictions on data availability

Source data are available for this paper, in the form of Excel files and raw image stacks (accession link: <http://doi.org/10.24631/ssbd.repos.2020.07.002>). All other data that support the plots within this paper and other findings of this study are available from the corresponding author upon reasonable request.

Field-specific reporting

Please select the one below that is the best fit for your research. If you are not sure, read the appropriate sections before making your selection.

Life sciences Behavioural & social sciences Ecological, evolutionary & environmental sciences

For a reference copy of the document with all sections, see nature.com/documents/nr-reporting-summary-flat.pdf

Life sciences study design

All studies must disclose on these points even when the disclosure is negative.

Sample size	No particular statistical method was used to predetermine the sample size. A minimum of n=3 independent experiments were performed based on previous studies in the field.
Data exclusions	No data exclusion
Replication	Experiments were reliably reproduced and were carried out on different days.
Randomization	Experiments mostly did not involve comparisons between groups and randomization is not relevant.
Blinding	Experiments mostly did not involve comparisons between groups and blinding is not relevant.

Reporting for specific materials, systems and methods

We require information from authors about some types of materials, experimental systems and methods used in many studies. Here, indicate whether each material, system or method listed is relevant to your study. If you are not sure if a list item applies to your research, read the appropriate section before selecting a response.

Materials & experimental systems

n/a	Involved in the study
<input checked="" type="checkbox"/>	Antibodies
<input type="checkbox"/>	Eukaryotic cell lines
<input checked="" type="checkbox"/>	Palaeontology and archaeology
<input checked="" type="checkbox"/>	Animals and other organisms
<input checked="" type="checkbox"/>	Human research participants
<input checked="" type="checkbox"/>	Clinical data
<input checked="" type="checkbox"/>	Dual use research of concern

Methods

n/a	Involved in the study
<input checked="" type="checkbox"/>	ChIP-seq
<input checked="" type="checkbox"/>	Flow cytometry
<input checked="" type="checkbox"/>	MRI-based neuroimaging

Eukaryotic cell lines

Policy information about [cell lines](#)

Cell line source(s) MDCK cells were purchased from the RIKEN BioResource Center (no. RCB0995).

Authentication Cell lines were authenticated by morphology check with microscopy

Mycoplasma contamination Mycoplasma testing was performed using PlasmoTest (InvivoGen) and cell lines were tested negative.

Commonly misidentified lines
(See [ICLAC](#) register) No commonly misidentified cells were used.

Supplementary information

Theory of mechanochemical patterning and optimal migration in cell monolayers

In the format provided by the
authors and unedited

Supplementary Information: Theory of mechano-chemical patterning and optimal migration in cell monolayers

I. MODEL DERIVATION

A. Equilibrium of cellular shape

We start by considering the equilibrium of a single cell, under differential tensions on its apical, lateral and basal areas (resp denoted γ_a , γ_l and γ_b). The energy of a single cell of height h and characteristic length l then reads [1–6]:

$$U = \gamma_l h l + (\gamma_a + \gamma_b) l^2 \quad (\text{S1})$$

Because we model 3D cells restricted to a flat substrate, we need only consider stable shapes with zero average spontaneous curvature such that apical and basal areas are equal. Moreover, epithelial cells may be considered incompressible, with constant volume $V_0 = h l^2$, given the small forces generated by actomyosin structures (compared to osmotic forces) [7], and since cell volume does not change appreciably over the time scales considered (minutes to hour). Minimizing the energy with respect to l provides the equilibrium shape of a given cell $l_0 = (\frac{V_0}{2} \frac{\gamma_l}{\gamma_a + \gamma_b})^{1/3}$, and expanding up to 2nd order around this minimum energy yields:

$$U(l) = U(l_0) + (l - l_0) U'(l_0) + \frac{(l - l_0)^2}{2!} U''(l_0) + \dots \quad (\text{S2})$$

$$= U(l_0) + \frac{(l - l_0)^2}{2!} U''(l_0) + \dots \quad (\text{S3})$$

$$\approx U(l_0) + k(l - l_0)^2, \quad (\text{S4})$$

which is the potential of a harmonic oscillator, valid for small perturbations around the equilibrium cell diameter l_0 . Computing the value of the second derivative at l_0 provides a value for the spring constant $k = 3(\gamma_a + \gamma_b)$. Such a linearization is valid as we find that the amplitude of oscillations in cell area are typically small compared to the average area (around 5 – 10%, see Extended Data Fig. 3a). Note that we discarded potential line tensions in this analysis, although this would not qualitatively affect the results as we are considering only small deviations from mechanical equilibrium. We also neglect the role of proliferation, as it occurs on much longer time scales than the period of the wave and is not required for wave formation in MDCK layers [8]. For now we also neglect visco-elasticity of the epithelial monolayer, which can arise from re-arrangements or

division/apoptosis events, but will incorporate it in Section II E as a sensitivity analysis to show that it does not qualitatively affect results.

Given the reported role in ERK/MAPK in regulating the actomyosin cytoskeleton [9, 10], one can in principle write a dependency of any tension γ_i on ERK activity. This means that the equilibrium length of a given cell will generically depend on ERK activity such that $l_0 = l_0(ERK)$. Recent experiments have indeed shown that varying ERK activity causes relative changes in F-Actin intensity between lateral and basal surfaces of MDCK cells [10]. We will next consider mechanical couplings between cells in monolayers and the interaction of ERK with mechanics. This description will account for differences in biochemical activities and mechanical properties in different biological settings which lead to differences in spatio-temporal dynamics of ERK activity.

B. Overdamped chain of mechano-chemical springs

A major function of epithelial tissues is to form tight barriers, which is achieved through strong mechanical couplings between neighbouring cells mediated by adhesion molecules such as E-Cadherin [11]. We write down a force balance equation for a cohesive 1D chain of epithelial cells, with cell i characterized by ERK activity $E_i(t)$ and delimited by vertices $r_i(t)$ and $r_{i+1}(t)$. For vertex r_i , which is under frictional contact with a substrate (modelled as fluid friction with coefficient ζ), this reads

$$\zeta(r_i(t+dt) - r_i(t)) = -k_i(r_i(t) - r_{i-1}(t) - l_i^0(t)) + k_{i+1}(r_{i+1}(t) - r_i(t) - l_{i+1}^0(t)) \quad (\text{S5})$$

where l_i^0 and k_i are the rest lengths and spring constants of a single cell and depend on 3D tensions as derived above. In the following, we will look only up to linear stability of the model so we discard the spatial variation in k_i which manifests as non-linear terms. In the continuum limit the vertex model becomes

$$\tau_r \partial_t r = \partial_{xx} r - \partial_x l^0. \quad (\text{S6})$$

Here, lengths have been scaled by a characteristic cell length $\langle l \rangle$ and we have defined a characteristic mechanical timescale $\tau_r = \zeta/k$. This timescale defines how quickly a mechanical stress diffuses in the monolayer - infinitely fast in the limiting case of vanishing friction, $\zeta \rightarrow 0$.

We now incorporate mechanosensation and response involving the chemical species ERK:

$$\begin{cases} \tau_r \partial_t r = \partial_{xx} r - \partial_x l_0 \\ \tau_l \partial_t l_0 = -(l_0 - l_0^{eq}) - \alpha(E - E_{eq}) \\ \tau_E \partial_t E = -(E - E_{eq}) + \beta \partial_x r \end{cases} \quad (\text{S7})$$

The second equation represents the tendency of the rest length towards an intrinsic equilibrium cell length and the action of ERK on decreasing rest length. The third equation represents decay of ERK towards an equilibrium activity, E_{eq} , and the action of increasing cell length ($l = \partial_x r \sim r_{i+1} - r_i$) on increasing ERK activation. Since ERK and rest lengths are carried within cells we could also write advection terms on l_0 and E with cell velocity $\partial_t r$. However, these terms would not affect the pattern forming behaviour that we wish to study since the linear stability around the homogeneous equilibrium state is unchanged. Alternatively, dropping advection terms is equivalent to assuming that waves of ERK and strain propagate fast compared to cell velocity which is valid for this system [9, 10]. Before proceeding it will help us to rewrite the model using the change of variables $l_0 \leftarrow l_0 - l_0^{eq}$ and $E \leftarrow E - E_{eq}$:

$$\begin{cases} \tau_r \partial_t r = \partial_{xx} r - \partial_x l_0 \\ \tau_l \partial_t l_0 = -l_0 - \alpha E \\ \tau_E \partial_t E = -E + \beta \partial_x r \end{cases} \quad (\text{S8})$$

Linear stability around the homogeneous fixed state yields the following dispersion relation:

$$(\tau_l \omega + 1)(\tau_E \omega + 1)(\tau_r \omega + q^2) = -\alpha \beta q^2 \quad (\text{S9})$$

From this we predict a patterning instability at the critical point defined by $Re[\omega] = 0$ and $\frac{dRe[\omega]}{dq} = 0$, which translates to:

$$\alpha \beta > (\alpha \beta)_{\text{crit}} = \frac{(\tau_E + \tau_l)(\sqrt{\tau_E} + \sqrt{\tau_l})^2}{\tau_E \tau_l} \quad (\text{S10})$$

The real and imaginary parts of ω at the critical point then define the wavenumber and angular frequency of the predicted instability, which read:

$$q_c^2 = \frac{\tau_r}{\sqrt{\tau_E \tau_l}}, \quad \omega_c^2 = \frac{1}{\tau_l^{1/2} \tau_E^{3/2}} + \frac{1}{\tau_l^{3/2} \tau_E^{1/2}} + \frac{1}{\tau_l \tau_E}. \quad (\text{S11})$$

Interestingly, both the wavelength and period of the instability are independent of the strength of the couplings α and β . Instead, they involve only the three time scales of the problem, which can

all be measured from macroscopic observation. Furthermore the period depends only on τ_l and τ_E and not on τ_r . For $\alpha\beta > 0$ this is expected since the system is just a classical activator-inhibitor with delay which generically produces temporal oscillations even in the absence of spatial couplings. The mechanical time scale τ_r affects only in the wavelength of the instability (see Extended Data Fig. 2a). Its role is clearest when considering the limiting case (valid experimentally as described below) of $\tau_E \ll \tau_l$. In this limit, the period of the instability scales as $T \propto \tau_E^{1/4} \tau_l^{3/4}$ so that the wavelength scales as

$$\lambda \propto \frac{T}{\sqrt{\tau_l \tau_r}}. \quad (\text{S12})$$

Here $\sqrt{\tau_l \tau_r}$ is the characteristic timescale of mechanical signal propagation upon biochemical change, so that the length scale of the instability is determined by how far a signal can propagate during a single temporal period of the mechano-chemical oscillation between ERK and cellular shape.

Although the linear instability threshold depends only on the product of mechano-chemical couplings $\alpha\beta$, the amplitude of mechanical vs. chemical fluctuations does depend on the relative values of couplings. We simulate the dynamics of the 1D system above the critical point ($\alpha\beta = 1.2 \times (\alpha\beta)_{\text{crit}}$) for different ratios $\alpha/\beta = 0.2, 1, 5$. As anticipated, cell shape is nearly un-affected for very small α while ERK levels vary drastically. In the reverse case of large α , small ERK oscillations are accompanied by major lattice deformations and cellular stretching (Extended Data Fig. 2b). Note that for numerical simulations of the model, we have to specify a non-linearity in the problem to prevent infinite activation of ERK. For this we took the simplest leading-order expansion on ERK activity:

$$\tau_E \partial_t E = -E - E^3 + \beta \partial_x r. \quad (\text{S13})$$

although other non-linearities (for instance on the rest length equation l_0) have similar consequences.

C. Active migration and direction sensing

Although the above theory reproduces ERK/density waves at an appropriate wavelength and period (see Main Text), the appearance of persistent directed waves in migrating monolayers remains to be understood theoretically, together with the biophysical mechanisms through which they might guide long-range active migration [10].

1. Incorporation of active migration in the model

To address this, we define a cell polarity p , a continuous variable taking both positive and negative values, which controls the direction and magnitude of active migration forces generated between cell and substrate (and thus the direction of active migration), and explore the influence of a coupling between local cell polarity p and gradients of stress $\partial_x \sigma_{xx} = \partial_x(\partial_x r - l_0)$, which is based on experimental evidence in multiple systems [12–16] (see Section II D for a discussion of alternative couplings). This gives us the following model:

$$\begin{cases} \tau_r \partial_t r = \partial_{xx} r - \partial_x l_0 + p \\ \tau_l \partial_t l_0 = -l_0 - \alpha E \\ \tau_E \partial_t E = -E + \beta \partial_x r \\ \tau_p \partial_t p = -p + D_p \partial_{xx} p - \gamma \partial_x \sigma_{xx} \end{cases} \quad (\text{S14})$$

where polarity feeds back on the first (force-balance) equation as an external traction force. The last equation is the simplest one can write on polarity, developing at linear order around a $p = 0$ state (which cells relax to in the absence of external stimuli/force). τ_p characterizes the time scale of polarity changes, the diffusion coefficient D_p represents possible short-range polarity alignment between neighboring cells, and γ controls the strength of coupling between gradients of stress and polarity [16].

Such a stress-polarity coupling has been shown to be mediated by Merlin [13], a mechano-sensitive protein that re-localizes from cortical cell-cell junctions to the cytoplasm in the presence of external forces during cell migration. This relocalization coordinates polarized Rac1 activity and lamellipodium formation, thus acting exactly as the γ parameter in linking gradients of stress from cell-cell contacts to traction forces. In Fig. 4, we thus use Merlin knock-outs to compare to model predictions for reduced γ . A further indication that the role of Merlin is mainly to modulate the γ parameter is that wavelengths and periods of the oscillations (which depend on τ_R , τ_l , τ_E) are unaffected in Merlin KO (Extended Data Fig. 9d).

Importantly however, this model still requires a non-linearity to break symmetry of wave propagation/cell migration directionality: without it polarity oscillates around mean zero, such that there is no long-range order and no persistent directional migration. In the main text we discuss experimental evidence that suggests traction forces are a decreasing function of ERK activity and use this to motivate a non-linearity on the coupling between polarity and gradients of stress $\gamma = \gamma(E)$ [10].

This addition allows phase differences between ERK and stress (which naturally exist and are fully generic to our mechano-chemical patterns) to control the degree of symmetry breaking (see Fig. 3c for a schematic). As mentioned in Section IA, ERK activity is observed to modulate the distribution of F-actin between the lateral and basal surfaces [10]. This indicates that ERK modulates (possibly in a related manner) both the relative surface tensions (and thus the stable cell shape/aspect ratio) as well as the polar traction forces from directional migration described here. The main difference between the two is that basal surface tension (either from cortical actomyosin or stress fibers) is a scalar term, which modulates the active stresses inside the monolayer, whereas directed migration forces are polar terms, which impact on the external forces exerted on/from the substrate. Strictly speaking traction forces have two active contributions: the first originating from gradients in scalar basal surface tensions and associated with changes in cell/tissue size; the second originating from directional actomyosin flows at basal surfaces. In what follows this latter contribution, proportional to the variable p , is what we refer to as traction force and we will be interested in how this term responds to mechano-chemical waves.

We analyse this in more detail below by assuming a simple saturating non-linearity of the form $\gamma(E) = \gamma/(1 + e^E)$, although all of our conclusions only require a variation of γ with E . It is useful to non-dimensionalize by $T = \tau_l$ and $L = a\sqrt{\tau_l/\tau_r}$ with a the average cell size (set to one), make the change of variables $E \leftarrow \alpha E$, $l_0 \leftarrow Ll_0$ and absorb parameters $\beta \leftarrow \alpha\beta$, $D_p \leftarrow D_p/L^2$, $\tau_E \leftarrow \tau_E/T$ and $\tau_p \leftarrow \tau_p/T$ so that the model reads

$$\begin{cases} \partial_t \sigma = \partial_{xx} \sigma + \partial_x p + l_0 + E \\ \partial_t l_0 = -l_0 - E \\ \tau_E \partial_t E = -E + \beta \partial_x r \\ \tau_p \partial_t p = -p + D_p \partial_{xx} p - \frac{\gamma}{1+e^{\frac{E}{\alpha}}} \partial_x \sigma. \end{cases} \quad (\text{S15})$$

To gain insight into this system we first derive analytical solutions for the response of an initially un-polarized tissue to an applied ERK wave (as performed for instance in Ref. [9] - although note the differences between our theory and the theory in Ref. [9], which neglected polarity, set $\tau_l \rightarrow 0$ and had a different sign $\alpha < 0$ for the length-ERK coupling to the one revealed by our optogenetic experiments, see Fig. 2c-f). We impose a right-left traveling ERK wave $E(x, t) = \cos(qx + \omega t)$ and assume that the traction term $\partial_x p$ can be neglected (an approximation which renders analytical expressions more tractable, and which we verify/relax in numerical simulations of the phase diagram of Fig. 3d). We also neglect diffusion of polarity ($D_p = 0$), which would otherwise act to soften

oscillations without qualitatively changing the results, leaving us with a relatively simple model which can be solved analytically:

$$\begin{cases} \partial_t \sigma = \partial_{xx} \sigma + l_0 + E \\ \partial_t l_0 = -l_0 - E \\ \tau_p \partial_t p = -p - \frac{\gamma}{1+e^{\alpha}} \partial_x \sigma. \end{cases} \quad (\text{S16})$$

For $l_0(x, t)$ and $\sigma(x, t)$ we find sinusoidal solutions:

$$l_0(x, t) = -\frac{1}{\sqrt{1+\omega^2}} \cos(qx + \omega t - \text{atan}(\omega)) \quad (\text{S17})$$

$$\sigma(x, t) = A_\sigma \cos(qx + \omega t + \phi_\sigma) \quad (\text{S18})$$

with A_σ and ϕ_σ given by

$$A_\sigma = \frac{1}{\sqrt{(1+\omega^2)(1+\frac{q^4}{\omega^2})}} \quad \phi_\sigma = \text{atan}\left(\frac{q^2-\omega^2}{\omega(1+q^2)}\right) \quad (\text{S19})$$

If we assume that $\gamma(E)$ is far from saturation we can use a linear approximation $\gamma(E) = \gamma(1/2 - E/(4\alpha))$ to obtain a solution also for the polarity:

$$\begin{aligned} p(x, t) = & -\frac{qA_\sigma}{8\alpha} \left(\sin(\phi_\sigma) + \frac{4\alpha}{\sqrt{1+\tau_p^2 w^2}} \cos[\omega t + qx + \phi_\sigma + \text{atan}(\frac{1}{\tau_p \omega})] \right. \\ & \left. - \frac{1}{\sqrt{1+4\tau_p^2 w^2}} \cos[2\omega t + 2qx + \phi_\sigma + \text{atan}(\frac{1}{2\tau_p \omega})] \right) \end{aligned} \quad (\text{S20})$$

Here, we see that symmetry is broken by the appearance of a constant term and that the shape of the oscillation is altered by the appearance of a phase-shifted second harmonic. The constant term is also the average polarity \bar{p} which is approached in the limit $\tau_p \rightarrow \infty$:

$$\bar{p}(\omega, q) = \lim_{\tau_p \rightarrow \infty} p(x, t | \omega, q) = -\frac{qA_\sigma(\omega, q)}{8\alpha} \sin(\phi_\sigma(\omega, q)) = \frac{1}{8\alpha} \frac{\omega q (\omega^2 - q^2)}{(1+\omega^2)(q^4 + \omega^2)} \quad (\text{S21})$$

2. Optimal polarization of the monolayer

Thus, the average polarity is determined by the angular frequency ω and wavenumber q of the applied wave (plotted in Extended Data Fig. 8a). From Eq. S21 we see that there is a boundary between net-positive and net-negative polarization at $\omega = q$.

Importantly, we find that polarity is maximized in the direction opposite to the ERK/density waves for a unique value of the wavelength and period of the wave. This allows us to define, as

discussed in the main text, an optimality criterion, for which the global average polarization of the monolayer is maximal (and given the fact that large-scale monolayer expansion arises from polarized migration forces in the tissue bulk [17], this also corresponds to waves inducing maximal displacement).

This optimality criteria corresponds to a phase difference $\phi_\sigma = \pi/4$ with ERK preceding stress (with the coefficient α changing only the value of the optimum and not its position). Since stress, $\sigma = \partial_x r - l_0$, involves the hidden variable l_0 it is more informative to compare the phase difference between cell length $\partial_x r$ and ERK (see Fig. 1d) for which we find that $\partial_x r$ precedes ERK by $\pi/4$ at optimum.

Analysis gives expressions for the optimal wavelength and period:

$$q = 1 \text{ and } \omega = 1 + \sqrt{2} \quad (\text{S22})$$

or adding back dimensions,

$$\lambda = 2\pi \sqrt{\frac{\tau_l}{\tau_r}} \text{ (in units of cell length)} \quad \text{and} \quad T = \frac{2\pi}{1 + \sqrt{2}} \eta \quad (\text{S23})$$

With experimentally estimated values of τ_r and τ_l (see Fig. 2 and note that τ_E does not appear because we are enforcing the dynamics on ERK) we predict optimal waves at wavelengths of 10–40 cells and periods of 2–10 hours (Extended Data Fig. 8a). However, this analytical criteria does not take into account ERK de-sensitisation, occurring on time scales of roughly an hour, which manifests in slow, long-term, decays of ERK activity following both mechanical stretch (Fig. 2b) and optogenetic ERK activation experiments [10]. We anticipate that this effect will decrease sensitivity to long-period oscillations and when we include it in numerical simulation of the full model ($\tau_d = 1$ h, see Section II A for further theoretical details), we see that the optimum moves towards shorter periods and wavelengths (albeit relatively little, displaying robustness of the results, see Fig. 3d and Extended Data Fig. 8). The predicted optimum then occurs at wavelengths of $\lambda \approx 15 - 30$ cells and periods of $T \approx 2 - 7$ hours.

3. Survey of wavelengths and periods observed in the literature

Strikingly, this predicted range is close to the values observed in multiple systems, including the MDCK cells which we study:

- In our conditions, (Fig. 3d and Extended Data Fig. 8) we find ranges, for confluent tissue $\lambda = 20 \pm 1$ cells $T = 108 \pm 3$ min and migrating tissue $\lambda = 21 \pm 5$ cells $T = 96 \pm 4$ min. Using

the range of estimates for τ_l , τ_r and τ_E we also plot the point $\lambda = 10_{-3}^{+6}$ cells $T = 70 \pm 20$ min sitting on the theoretical line from the dispersion relation (Eq. 5) from the main text (asymmetrical error bars appear on λ because upper and lower bounds depend non-linearly on the ranges of three different parameters - see Eq. 6 on the main text). Ref. [9, 10] also found ranges of $\lambda \approx 10 - 20$ cells, $T \approx 1 - 2$ h.

- In Ref. [8]: $\lambda \approx 50$ cells (our estimation from their report of a wavelength around 1mm and cell diameter of $20\mu\text{m}$), $T \approx 2$ h
- In Ref. [18]: $\lambda \approx 18$ cells (our estimation from their report of a wavelength of $370\mu\text{m}$ and cell diameter of $20\mu\text{m}$), $T \approx 4.7$ h. In Fig. 3d and Extended Data Fig. 8, we plot extracted ranges $\lambda = 18.5 \pm 1.5$ cells $T = 282 \pm 42$ min.
- In Ref. [19]: $T \approx 6$ h, and a wavelength of at least $700\mu\text{m}$ (as cells oscillate coherently on a $700\mu\text{m}$ diameter disk), i.e. approx 35 cells
- From figures in Ref. [20]: we estimate a period $T \approx 5$ h and a wavelength of $\lambda \approx 350\mu\text{m}$ (approx. 15-20 cells)
- From Ref. [21]: $T \approx 2.6$ h and a wavelength of $\lambda \approx 15$ cells (estimated combining their measurement of period with their estimation of propagation speed of the wave, leading to around $300\mu\text{m}$).
- In Ref. [22], which examines *in vivo* mouse skin upon wound healing, we went back to the data and estimated $\lambda \approx 8$ cells, $T \approx 1.3$ h. Point plotted in Fig. 3d and Extended Data Fig. 8.

We note that some discrepancies in the wavelength and period observed for MDCK cells are likely to be due to differences in experimental set-ups. Different substrates for instance are expected to modify the friction coefficient ζ of monolayers ($\tau_r = \zeta/k$), thus directly impacting the wavelength of the instability, as well as potentially affecting the time scales of ERK signalling (τ_E and τ_l) via mechano-sensation. However, it remains striking that our measurements, as well as published values of wavelength and period, indicate that the system is close to optimality in terms of polarization strength in response to a mechano-chemical wave.

Furthermore, although we have so far considered the limiting case of driven ERK dynamics (in which any wave can be applied on the system), the biophysical origin of the instability places

additional constraints on the system. In particular, it restricts the period and wavelength of the instability to a curve in $\omega - q$ space (i.e. the dispersion relation of our instability, see Fig. 3d or Extended Data Fig. 8). Interestingly, we find that the emergent waves possible from our biophysical model have dominant modes governed by $\omega^4 = q^4 + q^3 + q^2$ such that they can only induce polarization in the direction opposite to ERK propagation (i.e. sitting in the side of the diagram where $\omega > q$), for any values of model parameters! This makes it an extremely robust mechanism for coordinating cell migration in a unidirectional manner.

II. SENSITIVITY TO MODEL ASSUMPTIONS

In this section, we discuss different extensions to our model, as well as alternative couplings, to provide insights as to its robustness.

A. Adaptation of ERK to mechanical stresses

Our model for ERK dynamics (Eq. S8) can be extended to account for slow adaptation of ERK in response to constant stretch or long-term optogenetic activation ([10] and Fig. 2). In its simplest form, a model of long-term ERK adaption reads:

$$\tau_E \partial_t^2 E + \partial_t E = -E/\tau_d + \beta \partial_t \partial_x r. \quad (\text{S24})$$

As can be seen from the limiting case of this equation: on time-scales longer than τ_d , ERK relaxes towards zero (irrespective of cell area), whereas on time-scales shorter than τ_d , we recover the previous behavior, with ERK linearly following the deformation $\partial_x r$ with a delay τ_E . One can then recalculate the dispersion relation for this extended/adaptive model:

$$(\tau_E \omega^2 + \omega + 1/\tau_d)(\tau_l \omega + 1)(\tau_r \omega + q^2) = -\alpha \beta \omega q^2 \quad (\text{S25})$$

As expected this reduces to the previous dispersion relation for $\tau_d \rightarrow \infty$.

We estimated a lower bound on τ_d by fitting mechanical stretch experiments (Fig. 2a,b) with numerical solutions of Eq. S24 for an instantaneously applied constant stretch (temporal step function in $\partial_x r$ - see Extended Data Fig. 4c) and estimate $\tau_d \approx 1\text{h}$. Importantly, the dispersion relation for corresponding values of τ_d shows only slight differences (even for short de-sensitization time scales of $\tau_d = 30\text{min}$, Extended Data Fig. 4d), arguing that adaptation has a negligible effect on pattern formation in this system. One should note however that adaptation should be important for

longer-term expansion experiments on time scale of days, although in this case other effects such as cell division [8, 23] also become important. We also discussed above (Section IC) how adaptation slightly reduces the effectiveness of very-long period (and wavelength) waves for inducing strong polarization (see Extended Data Fig. 8).

B. Direct cell-cell biochemical communication

In our model, ERK is restricted to the subcellular level, and does not diffuse directly from one cell to the next, instead propagating via mechanical couplings and the mechano-sensitivity of ERK (which is validated by the analysis of the experiments of Fig. 2 and [10]). An extension could consider that biochemical relays act as an effective diffusion coefficient D_E appearing directly in the equation on ERK dynamics:

$$\tau_E \partial_t E = \tau_E D_E \partial_{xx} E - E + \beta \partial_x r. \quad (\text{S26})$$

This allows for diffusive biochemical communication over the lengthscale $\sqrt{D_E \tau_E}$ and translates into a modified dispersion relation:

$$(\tau_E \omega + 1 + D_E q^2)(\tau_l \omega + 1)(\tau_r \omega + q^2) = -\alpha \beta q^2 \quad (\text{S27})$$

Plotting this dispersion relation for $D_E = 1$, a typical diffusion rate for biological proteins given the Stokes-Einstein equation ($D_E \approx 10 \mu\text{m}^2 \text{s}^{-1}$ in real units for cell length $< l > \approx 20 \mu\text{m}$), shows that if present this would have only very weak effects on the instability and pattern formation (Extended Data Fig. 4b).

C. Alternative couplings of ERK to cell strain

In principle, ERK could also respond to cell strain or strain rate, rather than absolute cell length (as is assumed and main text, and used to fit the mechanical stretching experiment). For a coupling to cell strain the model becomes

$$\begin{cases} \tau_r \partial_t r = \partial_{xx} r - \partial_x l_0 \\ \tau_l \partial_t l_0 = l_0^{eq} - l_0 - \alpha E \\ \tau_E \partial_t E = -E + \beta(\partial_x r - l_0) \end{cases} \quad (\text{S28})$$

with the following dispersion relation resulting from linear stability

$$(\tau_l\omega + 1)(\tau_E\omega + 1)(\tau_r\omega + q^2) = \alpha\beta\tau_r\omega \quad (\text{S29})$$

With increasing $\alpha\beta$ the system first becomes unstable at infinite wavelength with no oscillatory component (an exponentially growing homogeneous instability). Therefore, this alternative coupling cannot explain the patterns seen in data. Similarly, we consider the following couplings to strain rate, defined either on absolute cell size or with reference to the cells rest length:

$$\begin{cases} \tau_r\partial_t l = \partial_{xx}(l - l_0) \\ \tau_l\partial_t l_0 = l_0^{eq} - l_0 - \alpha E \\ \tau_E\partial_t E = -E + \beta\partial_t l \end{cases} \quad (\text{S30})$$

and

$$\begin{cases} \tau_r\partial_t l = \partial_{xx}(l - l_0) \\ \tau_l\partial_t l_0 = l_0^{eq} - l_0 - \alpha E \\ \tau_E\partial_t E = -E + \beta\partial_t(l - l_0) \end{cases} \quad (\text{S31})$$

which give the dispersion relations

$$(\tau_l\omega + 1)(\tau_E\omega + 1)(\tau_r\omega + q^2) = -\alpha\beta\omega q^2 \quad (\text{S32})$$

and

$$(\tau_l\omega + 1)(\tau_E\omega + 1)(\tau_r\omega + q^2) = \alpha\beta\tau_r\omega^2 \quad (\text{S33})$$

The first case is always stable for $\alpha\beta > 0$ and the second shows similar behaviour to the previous coupling to strain (Eq. S29). This rules out couplings to strain and strain rate as an explanation for the patterns seen data, consistent also with mechanical perturbation experiments, where an almost instantaneous strain is applied (Fig. 2b). A coupling between ERK and absolute cell size is therefore the simplest coupling that can describe the patterns seen in data.

D. Alternative coupling of polarity to local velocity

In the main text, we explore the influence of a coupling between local cell polarity p and gradients of stress, which is based on experimental evidence in multiple systems [12–16]. There are, however,

other proposals for how tissue mechanics impacts cellular polarity, and in particular the possibility that cellular polarity \vec{p} aligns with cellular velocity \vec{v} (which are not necessarily identical in confluent monolayers due to mechanical couplings between cells [16, 24]). This would modify the equation for polarity in Eq. S14 as follows:

$$\tau_p \partial_t p = -p + D_p \partial_{xx} p + \gamma v \quad (\text{S34})$$

Notice however that gradients of stress and cell velocity $v = \partial_t r$ are closely related by force balance:

$$\tau_r \partial_t r = \partial_x \sigma_{xx} + p \quad (\text{S35})$$

such that re-injecting velocity into Eq. S34 returns a term on gradients of stress:

$$\tau_p \partial_t p = -(1 - \frac{\gamma}{\tau_r})p + D_p \partial_{xx} p + \frac{\gamma}{\tau_r} \partial_x \sigma_{xx}. \quad (\text{S36})$$

This term is similar, up to a rescaling factor, to the coupling assumed in main text but with opposite sign. This sign difference is important because it reverses the direction in which cells polarize in response to ERK waves, i.e. polarity-velocity coupling produces migration in the opposite direction compared to the model in the main text (stable only as long as $\gamma < 1$.) All of the conclusions regarding optimality are therefore reversed and emergent waves robustly produce polarity in the “wrong” direction, leading us to favour our original coupling. Finally, considering a direct polarity alignment between cells (modelled as a diffusion coefficient D_p in the polarity equation), does not change qualitatively any of the results discussed in the main text so we omit it in simulations.

E. Visco-elasticity

On long time scales the viscous properties of cells and tissues become important and we can modify our system of equations to determine whether this has any effect on our predictions for pattern formation. In the elastic limit it is equivalent to consider either an ERK-dependent active stress $\sigma_a(ERK)$ or an ERK-dependent reference length $l_0(ERK)$. However, these two approaches are not equivalent for a viscoelastic material (c.f. creep vs stress relaxation). We therefore begin by reformulating our model in terms of an active stress before incorporating viscosity for each of the two cases.

1. ERK-dependent active stress in an elastic medium

For an active system we can decompose total stress into passive and active parts

$$\sigma = \sigma_p + \sigma_a \quad (\text{S37})$$

For an elastic medium the passive stress is related to the strain by Hooke's law

$$\sigma_p = \sigma - \sigma_a = k\epsilon \quad (\text{S38})$$

where k is the stiffness and ϵ is strain. Combining force balance between substrate friction and gradients of stress $\partial_x \sigma = \zeta v$ with the equation for strain rate $\dot{\epsilon} = \partial_x v$ gives

$$\partial_{xx} \sigma = \zeta \partial_x v = \zeta \dot{\epsilon} \quad (\text{S39})$$

Using the constitutive equation to eliminate σ gives us an equation of motion relating strain and active stress

$$\zeta \dot{\epsilon} = k \partial_{xx} \epsilon + \partial_{xx} \sigma_a \quad (\text{S40})$$

Once again, we incorporate mechano-sensitive ERK, which we take to depend on absolute cell length $l \sim (1 + \epsilon)$, to give a second dynamic equation

$$\tau_E \dot{E} = (E_{eq} - E) + \beta(1 + \epsilon) \quad (\text{S41})$$

Comparing with our previous model using the connection $l = (1 + \partial_x r) = (1 + \epsilon)$ shows that $\sigma_a = -kl_0$ and allows us to write a final dynamic equation for active stress

$$\tau_\sigma \dot{\sigma}_a = \sigma_a^{eq} - \sigma_a + \alpha(E - E_{eq}) \quad (\text{S42})$$

As expected, this gives an identical result to the one coarse-grained from the 3D vertex and spring model and presented in the Main Text. While this shows that there is no difference between active stress and an active rest length in the elastic limit, we discuss below that these cases need to be considered separately in visco-elastic models, or in models with a non-linear ERK-dependent stiffness (see Section II F).

2. ERK-dependent active stress in a visco-elastic medium

On timescales longer than cell re-arrangements (or division/apoptosis) biological tissues can be described as visco-elastic Maxwell fluids, and we thus use a classical Maxwell rheology as a starting

point given by the following constitutive equation

$$\frac{\dot{\sigma}_p}{k} + \frac{\sigma_p}{\eta} = \dot{\epsilon} \quad (\text{S43})$$

with η the viscosity of the tissue and other variables defined as in the section above. Using force balance ($\partial_{xx}\sigma_p = \zeta\dot{\epsilon} - \partial_{xx}\sigma_a$) to eliminate σ_p gives an equation of motion relating strain to active stress

$$\zeta\ddot{\epsilon} + \left(\frac{\zeta}{\tau_m} - k\partial_{xx}\right)\dot{\epsilon} = \partial_{xx}\dot{\sigma}_a + \frac{1}{\tau_m}\partial_{xx}\sigma_a \quad (\text{S44})$$

with $\tau_m = \eta/k$ a visco-elastic timescale. This modifies our system of equations as follows:

$$\begin{cases} \tau_r\ddot{\epsilon} + \left(\frac{\tau_r}{\tau_m} - \partial_{xx}\right)\dot{\epsilon} = \partial_{xx}\dot{\sigma}_a + \frac{1}{\tau_m}\partial_{xx}\sigma_a \\ \tau_l\dot{\sigma}_a = -\sigma_a + \alpha E \\ \tau_E\dot{E} = -E + \beta\epsilon \end{cases} \quad (\text{S45})$$

which reduces, as expected, to the elastic model described above for $\tau_m \rightarrow \infty$. Linear stability around the stationary state now gives the following dispersion relation

$$(\tau_l\omega + 1)(\tau_E\omega + 1)(\tau_r\omega + q^2 + \frac{\tau_r}{\tau_m}) = -\alpha\beta q^2(1 + \frac{1}{\tau_m\omega}) \quad (\text{S46})$$

Comparing to Eq. S9, and using the measured values of the period and wavelength $T = 90$ min and $\lambda = 20$ cells and the fitted value of $\tau_r = 10$ min, we can estimate that visco-elasticity will qualitatively modify the dispersion relation only when $\tau_m < \tau_r/(q^2 + \tau_r\omega) = 13$ min or $\tau_m < 1/\omega = 14$ min. These are much smaller than typical values of $\tau_m = 60$ min [8], and plotting (Extended Data Fig. 4e) for such values confirms that viscosity has little effect on the dispersion relation or initial patterning, justifying the approximations made in the main text.

3. ERK dependent rest length in a visco-elastic medium

For completeness we also study the case of an ERK dependent rest length in a visco-elastic medium. The previous constitutive equation for the elastic limit, $\sigma/k = \epsilon - l_0$, is replaced by

$$\frac{\dot{\sigma}}{k} + \frac{\sigma}{\eta} = \dot{\epsilon} - \dot{l}_0 \quad (\text{S47})$$

where we now consider a non-constant reference state l_0 instead of active stresses. Combining this with force balance ($\zeta\dot{\epsilon} = \partial_{xx}\sigma$) provides the following system of equations:

$$\begin{cases} \tau_r \ddot{\epsilon} + \frac{\tau_r}{\tau_m} \dot{\epsilon} = \partial_{xx}(\dot{\epsilon} - \dot{l}_0) \\ \tau_l \dot{l}_0 = -l_0 - \alpha E \\ \tau_E \dot{E} = -E + \beta \epsilon \end{cases} \quad (\text{S48})$$

The dispersion relation from a linear stability analysis is

$$(\tau_l \omega + 1)(\tau_E \omega + 1)(\tau_r \omega + q^2 + \frac{\tau_r}{\tau_m}) = -\alpha \beta q^2 \quad (\text{S49})$$

which again reduces, as expected, to the results of the main text for $\tau_m \rightarrow \infty$. As for the case of an ERK dependent active stress (Eq. S46) viscosity has little effect on patterning for realistic values of τ_m .

F. Alternative non-linear couplings for symmetry breaking

In order to break symmetry and produce a net traction force, we introduced a non-linear ERK dependency to the coefficient $\gamma(ERK)$ for the coupling between polarity and gradients of stress (see Section IC1). This was supported by observations of lower traction forces in cells upon optogenetic ERK activation [10].

However, we also wish to explore the impact of alternative non-linearities on symmetry-breaking. The first case that we consider is a non-linearity on the traction force $f_+(E)$ (which we had previously set to one without loss of generality as it could be absorbed upon non-dimensionalization within the polarity). Indeed, because the observations of Ref. [10] were on traction forces, this feedback could conceivably occur in force generation, rather than in polarization, $\gamma_+(ERK)$, so we again consider a decreasing function $f_+(E)$ for which we keep the same form, $f_+(E) = 1/(1 + \exp[E])$. The system of equations, non-dimensionalized as in Eq. S15, becomes

$$\begin{cases} \partial_t r = \partial_{xx} r + \partial_x \sigma_a + f_+[E] p \\ \partial_t \sigma_a = -\sigma_a + E \\ \tau_E \partial_t E = -E + \beta \partial_x r \\ \tau_p \partial_t p = -p - \gamma (\partial_{xx} r + \partial_x \sigma_a) \end{cases} \quad (\text{S50})$$

In the limit $\tau_p \rightarrow 0$ traction forces are identical to the case of a non-linearity on $\gamma(E)$, however symmetry in polarity remains nearly unbroken. We demonstrate this in Extended Data Fig. 7b

where we simulate the system with an applied ERK wave and measure how the net traction force depends on the period and wavelength of this wave. We also plot the spatial profile of the traction force $f_+(E)p$ (red) and cell polarity p (grey dashed) at the point indicated on the diagram. In these simulations we used a lower estimate of τ_p so that we compare the cases of $\gamma(E)$ (Extended Data Fig. 7a) and $f_+(E)$ when they are most similar. The traction forces are nearly identical in both the diagrams and spatial profiles. However, whereas for $\gamma(E)$ the profiles of polarity and traction force are identical (bar a rescaling) and show the same degree of symmetry breaking, for $f_+(E)$ the polarity profile differs greatly from its respective traction force profile and shows close to zero symmetry breaking. Since symmetry-breaking observed in data occurs both on polarity and traction forces (Fig. 3a and [10])), we rule out such a coupling on $f_+(E)$ in favour of $\gamma(E)$.

The second case assumes a non-linearity in the stiffness $k(E)$, which has differing effects depending on whether an ERK dependent active stress or ERK dependent rest length is considered (see also Section II E for a comparison of these two cases in the context of viscoelasticity). From the derivation of l_0 and k in terms of active surface tensions in Section I A, such a non-linearity can occur as k depends on cellular tensions which can be modified by ERK, and we accordingly consider it as an increasing function of ERK, using again a sigmoidal dependency $k(E) = kf_-(E) = k/(1+\exp[-E])$. For the first sub-case of an ERK dependent stiffness with an active reference length the system of equations becomes

$$\begin{cases} \partial_t r = f_-[E] (\partial_{xx} r - \partial_x l_0) + p \\ \partial_t l_0 = -l_0 - E \\ \tau_E \partial_t E = -E + \beta \partial_x r \\ \tau_p \partial_t p = -p - \gamma (\partial_{xx} r - \partial_x l_0) \end{cases} \quad (\text{S51})$$

Here, we find an inverse diagram (Extended Data Fig. 7c) with net polarization and traction force in the opposite direction compared to $\gamma(E)$ (Extended Data Fig. 7a). This coupling is therefore inconsistent with experimental observations. An even more dramatic difference occurs for the second sub-case of an ERK dependent stiffness with an active stress (note that $\sigma_a \sim -l_0$ for the an elastic

medium with a constant stiffness):

$$\begin{cases} \partial_t r = f_-[E] \partial_{xx} r + \partial_x \sigma_a + p \\ \partial_t \sigma_a = -\sigma_a + E \\ \tau_E \partial_t E = -E + \beta \partial_x r \\ \tau_p \partial_t p = -p - \gamma (\partial_{xx} r + \partial_x \sigma_a) \end{cases} \quad (\text{S52})$$

Net-polarisation and traction force is zero or positive (i.e. counter to ERK) for all wavelengths and periods but with an optimum located at very short wavelength and long period (Extended Data Fig. 7d). The degree of symmetry breaking is small in regions corresponding to observed waves which seems to rule this out as a mechanism for inducing net active migration in our biological setting.

We note that the different non-linearities in the cases presented here do not affect the linear stability determining pattern formation or modify the timescales estimated in the main text. The simulations in Extended Data Fig. 7 make use of these timescales (τ_l and τ_r were used to non-dimensionalize) and therefore offer a fair comparison between models. Other parameters were set throughout as $\gamma = 0.1$ and $\tau_p = 15$ min (β does not feature for an applied ERK wave). Finally, a proposed alternative [9] was to have a non-linear cell viscosity (effectively non-linear τ_r in our framework) which decreased with ERK. Although this produced symmetry-breaking in the correct direction, it relied on an instantaneous relationship between cell rest length and ERK, which corresponds to a simplification of $\tau_l \rightarrow 0$ in our model, as well as negative α - rather than positive when assessed by optogenetic experiments.

References

- [1] Okuda, S., Inoue, Y., and Adachi, T. (2015). Three-dimensional vertex model for simulating multicellular morphogenesis. *Biophysics and physicobiology*, 12, 13-20.
- [2] Krajnc, M., Storgel, N., Brezavsek, A. H., and Zihlerl, P. (2013). A tension-based model of flat and corrugated simple epithelia. *Soft Matter*, 9(34), 8368-8377.
- [3] Osterfield, M., Du, X., Schüpbach, T., Wieschaus, E., and Shvartsman, S. Y. (2013). Three-dimensional epithelial morphogenesis in the developing Drosophila egg. *Developmental cell*, 24(4), 400-410.
- [4] Hannezo, E., Prost, J. and Joanny, J.F., 2014. Theory of epithelial sheet morphology in three dimensions. *Proceedings of the National Academy of Sciences*, 111(1), pp.27-32.

- [5] Alt, S., Ganguly, P., and Salbreux, G. (2017). Vertex models: from cell mechanics to tissue morphogenesis. *Philosophical Transactions of the Royal Society B: Biological Sciences*, 372(1720), 20150520.
- [6] Fouchard, J., Wyatt, T.P., Proag, A., Lisica, A., Khalilgharibi, N., Recho, P., Suzanne, M., Kabla, A. and Charras, G., 2020. Curling of epithelial monolayers reveals coupling between active bending and tissue tension. *Proceedings of the National Academy of Sciences*, 117(17), pp.9377-9383.
- [7] Salbreux, G., Charras, G., and Paluch, E. (2012). Actin cortex mechanics and cellular morphogenesis. *Trends in cell biology*, 22(10), 536-545.
- [8] Tlili, S., Gauquelin, E., Li, B., Cardoso, O., Ladoux, B., Delanoe-Ayari, H. and Graner, F., 2018. Collective cell migration without proliferation: density determines cell velocity and wave velocity. *Royal Soc. Open Sci.*, 5(5), p.172421.
- [9] Aoki, K., Kondo, Y., Naoki, H., Hiratsuka, T., Itoh, R.E. and Matsuda, M., 2017. Propagating wave of ERK activation orients collective cell migration. *Dev. Cell*, 43(3), pp.305-317.
- [10] Hino, N., Rossetti, L., Marín-Llauradó, A., Aoki, K., Trepaut, X., Matsuda, M. and Hirashima, T., 2020. ERK-mediated mechanochemical waves direct collective cell polarization. *Developmental Cell*, 53(6), pp.646-660.
- [11] Heisenberg, C.P. and Bellaïche, Y., 2013. Forces in tissue morphogenesis and patterning. *Cell*, 153(5), pp.948-962.
- [12] Weber, G. F., Bjerke, M. A., and DeSimone, D. W. (2012). A mechanoresponsive cadherin-keratin complex directs polarized protrusive behavior and collective cell migration. *Developmental cell*, 22(1), 104-115.
- [13] Das, T., Safferling, K., Rausch, S., Grabe, N., Boehm, H., and Spatz, J. P. (2015). A molecular mechanotransduction pathway regulates collective migration of epithelial cells. *Nature cell biology*, 17(3), 276.
- [14] Scarpa, E., Szabo, A., Bibonne, A., Theveneau, E., Parsons, M., and Mayor, R. (2015). Cadherin switch during EMT in neural crest cells leads to contact inhibition of locomotion via repolarization of forces. *Developmental cell*, 34(4), 421-434.
- [15] Zimmermann, J., Camley, B. A., Rappel, W. J., and Levine, H. (2016). Contact inhibition of locomotion determines cell-cell and cell-substrate forces in tissues. *Proceedings of the National Academy of Sciences*, 113(10), 2660-2665.
- [16] Alert, R., and Trepaut, X. (2019). Physical Models of Collective Cell Migration. *Annual Review of Condensed Matter Physics*, 11.
- [17] Trepaut, X., Wasserman, M.R., Angelini, T.E., Millet, E., Weitz, D.A., Butler, J.P. and Fredberg, J.J., 2009. Physical forces during collective cell migration. *Nature physics*, 5(6), pp.426-430.
- [18] Petrolli, V., Le Goff, M., Tadrous, M., Martens, K., Allier, C., Mandula, O., ... and Cappello, G. (2019). Confinement-Induced Transition between Wavelike Collective Cell Migration Modes. *Phys. Rev. Lett*, 122(16), 168101.

- [19] Notbohm, J., Banerjee, S., Utuje, K.J., Gweon, B., Jang, H., Park, Y., Shin, J., Butler, J.P., Fredberg, J.J. and Marchetti, M.C., 2016. Cellular contraction and polarization drive collective cellular motion. *Biophys. J.*, 110(12), pp.2729-2738.
- [20] Serra-Picamal, X., Conte, V., Vincent, R., Anon, E., Tambe, D.T., Bazellieres, E., Butler, J.P., Fredberg, J.J. and Trepaut, X., 2012. Mechanical waves during tissue expansion. *Nature Physics*, 8(8), pp.628-634.
- [21] Rodriguez-Franco, P., Brugues, A., Marin-Llaurado, A., Conte, V., Solanas, G., Batlle, E., Fredberg, J.J., Roca-Cusachs, P., Sunyer, R. and Trepaut, X., 2017. Long-lived force patterns and deformation waves at repulsive epithelial boundaries. *Nature materials*, 16(10), pp.1029-1037.
- [22] Hiratsuka, T., Fujita, Y., Naoki, H., Aoki, K., Kamioka, Y. and Matsuda, M., 2015. Intercellular propagation of extracellular signal-regulated kinase activation revealed by *in vivo* imaging of mouse skin. *Elife*, 4, p.e05178.
- [23] Ranft, J., Basan, M., Elgeti, J., Joanny, J.F., Prost, J. and Jülicher, F., 2010. Fluidization of tissues by cell division and apoptosis. *Proceedings of the National Academy of Sciences*, 107(49), pp.20863-20868.
- [24] Basan, M., Elgeti, J., Hannezo, E., Rappel, W.J. and Levine, H., 2013. Alignment of cellular motility forces with tissue flow as a mechanism for efficient wound healing. *Proceedings of the National Academy of Sciences*, 110(7), pp.2452-2459.